Contrib Mineral Petrol (2015) 169:31
DOI 10.1007/s00410-015-1126-7

ORIGINAL PAPER

Episodic refertilization and metasomatism of Archean mantle: evidence from an orogenic peridotite in North Qaidam (NE Tibet, China)

Qing Xiong · William L. Griffin · Jian-Ping Zheng · Suzanne Y. O'Reilly · Norman J. Pearson

Received: 5 November 2014 / Accepted: 23 February 2015 / Published online: 7 March 2015

Abstract Episodic refertilization and metasomatism of depleted subcontinental lithospheric mantle (SCLM) is rarely revealed within a single orogenic peridotite. We have investigated the Shenglikou peridotite massif in the North Qaidam Orogen (NE Tibet, China) to understand its origin and secular re-enrichment history and possible links with global tectonism, using multiple chemical and isotopic techniques. The massif contains two main groups of rocks, one rich in olivine (Ol) and the other rich in pyroxene (Pyro). In situ Re–Os isotope analyses on sulfides and previous reported whole-rock Os data show the Shenglikou peridotite massif has an Archean origin. The Ol-rich group has Mg# up to 0.923, Al_2O_3 contents down to 0.55 wt%, low FeO contents, whole-rock HREE ~0.01–0.1 times chondritic values and high spinel Cr# (up to 0.71). Modeling suggests that the Ol-rich peridotites are residues after ~30–40 % melt extraction at ~1600–1500 °C and ≤5 GPa. Mineral compositions, oxygen-isotope compositions ($\delta^{18}O_{V\text{-}SMOW} = 5.7 \pm 0.1$ ‰) and attainment of Hf-isotope internal equilibration at ~1.5–1.4 Ga with initial ratios similar to that of depleted convective mantle indicate that the Ol-rich group was refertilized by silicate melts derived from the depleted asthenosphere at ~1.5–1.4 Ga, corresponding to one phase in the breakup of the Columbia supercontinent. On the other hand, chemical compositions and Hf–O isotopic signatures of the pyroxene-rich rocks suggest a second refertilization superimposed on the Archean lithospheric mantle at ~700 Ma, coeval with the global extension that affected Rodinia. Both groups show metasomatism by fluids, sourced from subducting slabs during the early Paleozoic convergence between the Qaidam and Qilian blocks. This study shows that the episodic refertilization and metasomatism of depleted Archean SCLM, temporally linked to supercontinental cycles, can be revealed in a single orogenic peridotite, and suggests that continental extension and convergence play an important role in the destruction of cratonic keels.

Keywords Orogenic peridotite · Sr–Nd–Hf–Os–O isotopes · Mantle refertilization and metasomatism · Supercontinental cycles · North Qaidam Orogen · Lithosphere evolution of northeastern Tibet

Communicated by Timothy L. Grove.

Electronic supplementary material The online version of this article (doi:10.1007/s00410-015-1126-7) contains supplementary material, which is available to authorized users.

Q. Xiong (✉) · J.-P. Zheng (✉)
State Key Laboratory of Geological Processes and Mineral Resources, Faculty of Earth Sciences, China University of Geosciences, Wuhan 430074, China
e-mail: qing.xiong1986@gmail.com; qing.xiong@mq.edu.au

J.-P. Zheng
e-mail: jpzheng@cug.edu.cn

Q. Xiong · W. L. Griffin · S. Y. O'Reilly · N. J. Pearson
ARC Centre of Excellence for Core to Crust Fluid Systems (CCFS) and GEMOC National Key Centre, Department of Earth and Planetary Sciences, Macquarie University, Sydney, NSW 2109, Australia

Introduction

Understanding of the formation and evolution of SCLM is a fundamental theme in solid-Earth science (e.g., Jordan 1978; Downes 2001; O'Reilly et al. 2001; Pearson et al. 2003; Griffin et al. 2003, 2009; Canil 2004; Carlson et al. 2005; Foley 2008; Pearson and Wittig 2008; Lee et al. 2011). The chemical buoyancy and thermal properties of

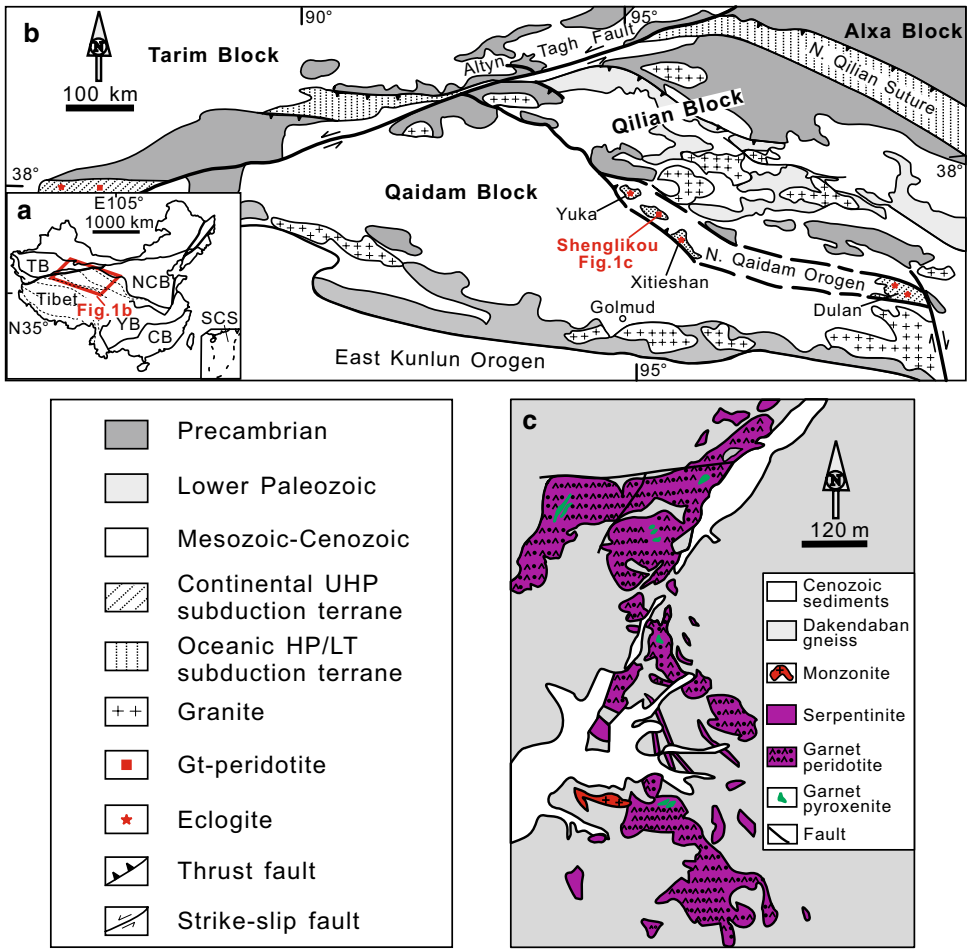

Fig. 1 Major tectonic units of China (**a**) and NE Tibet (**b**), and geological sketch maps of the Shenglikou peridotite massif (**c**) in the North Qaidam Orogen [modified after Xiong et al. (2014)]. *TB* Tarim Block, *NCB* North China Block, *YB* Yangtze Block, *CB* Cathaysia Block, *SCS* South China Sea, *N. Qaidam* North Qaidam, *N. Qilian* North Qilian

Archean SCLM determine its strength, stability and longevity relative to the Phanerozoic lithospheric mantle (Zheng et al. 2015). However, refertilization and metasomatism can modify and even destroy the refractory SCLM keels, through chemical erosion by melts/fluids from the underlying asthenosphere and subducting slabs or during mechanical collision with surrounding plates, as illustrated by the fate of the North China craton (e.g., Zheng et al. 1998, 2001, 2007, 2014; Xu 2001; Gao et al. 2002; Zhang 2005).

Peridotite massifs tectonically emplaced in orogenic belts usually retain kilometer- to centimeter-scale information on the processes that modify the SCLM (e.g., Bodinier and Godard 2003; Zheng et al. 2005, 2008; Beyer et al. 2006; Spengler et al. 2006; Le Roux et al. 2007; Liou et al. 2007). The diversity and heterogeneity in terms of chemical and isotopic compositions within a single orogenic peridotite can make the mantle origin and the sequence of re-enrichment events quite ambiguous. Moreover, although the growth and reworking of continental crust have been widely linked with supercontinental cycles (e.g., Condie 1998; Hawkesworth and Kemp 2006), there is less evidence on the possible relationships between SCLM modification (refertilization and metasomatism) processes and global tectonism.

The Shenglikou peridotite massif in the North Qaidam ultrahigh-pressure (UHP) belt, NE Tibet of western China is a complex ultramafic body (Fig. 1), with a variety of lithologies (dunite, harzburgite, lherzolite, wehrlite and pyroxenite) and isotopic compositions (e.g., Song et al. 2007, 2009; Yang and Powell 2008; Shi et al. 2010; Xiong et al. 2011, 2014). This complexity has produced debates on its origin (SCLM *vs* high-MgO cumulates), its early Paleozoic metamorphic and tectonic history (Song et al. 2004, 2005a, b, 2009; Yin et al. 2007a; Yang and Powell 2008) and the nature and timing of the metasomatic processes that have modified it (Song et al. 2007, 2009; Yang and Powell 2008; Shi et al. 2010; Xiong et al. 2011, 2014; Jung et al. 2013). However, there have not been any detailed studies that use multiple geochemical and isotopic techniques to reveal the mantle history of the Shenglikou peridotite massif prior to the early Paleozoic UHP recrystallization.

In this study, we have, for the first time, integrated analyses of the major- and trace-element compositions of minerals and whole-rock samples, and the Sr–Nd–Hf–Os–O isotopic compositions of minerals, from representative

lithologies in the Shenglikou peridotite massif. The aims are (1) to constrain the mantle origin of the massif, (2) to reveal the episodic mantle refertilization processes and their possible connection with global tectonism and (3) to evaluate the effect of fluid metasomatism on the SCLM during the early Paleozoic convergence between the Qaidam and Qilian blocks.

Geological setting

The North Qaidam Orogen (NQO) is a WNW-trending tectonic ribbon, formed by the early Paleozoic collision between the Qaidam and Qilian blocks. This orogeny represents one of the significant phases in the assembly of NE Tibet, which is presently bounded by the Tarim, North China and Yangtze cratons (Yin and Harrison 2000; Fig. 1a). The Qaidam block is covered by Mesozoic–Cenozoic sediments (south of the NQO; Fig. 1b); its crystalline basement is suggested to be Archean and to have experienced episodes of magmatism and tectonism in the Meso-Neoproterozoic, early Paleozoic and Mesozoic periods (e.g., Yin et al. 2007b; Xiong et al. 2011, 2012; Song et al. 2014). The Qilian block to the north of the NQO includes, from south to north, the Neoarchean–Paleoproterozoic Quanji micro-continent, the early Paleozoic South Qilian arc-accretionary complex and the Precambrian Central Qilian micro-continent (Chen et al. 2009a; Xiao et al. 2009; Song et al. 2014). Geological, geochemical and geochronological studies of the supracrustal rocks suggest that the two blocks experienced widespread magmatism and metamorphism related to the development of the Columbia to Rodinia supercontinents (e.g., Chen et al. 2009a; Song et al. 2010, 2012; Xiong et al. 2012). The early Paleozoic convergence between the Qaidam and Qilian blocks progressed from "Andean-type" oceanic subduction to subsequent "Himalayan-type" continental collision (e.g., Song et al. 2006, 2014; Xiong et al. 2012, 2014). The collision produced and exhumed masses of ultrahigh-pressure (UHP) crustal rocks from the deeply subducted Qaidam slab and rare fragments of mantle-wedge material from the Qilian lithosphere (e.g., Yang et al. 2002; Mattinson et al. 2006; Song et al. 2004, 2005a, b, 2006, 2007, 2009, 2014; Yin et al. 2007a; Yang and Powell 2008; Zhang et al. 2008a, b, 2010; Chen et al. 2009b; Xiong et al. 2011, 2012, 2014).

The UHP rocks occur as four discontinuous exposures in the North Qaidam Orogen (Dulan, Xitieshan, Shenglikou and Yuka; Fig. 1b). Ortho- and para-gneisses of the Proterozoic Dakendaban Group dominate the UHP exposures; minor eclogites, mafic granulites, amphibolites and peridotites are enclosed by the gneisses. Ortho- and para-gneisses are derived mainly from sedimentary material, which contained detrital zircons with U–Pb ages from Neoarchean to early Paleozoic (e.g., Song et al. 2006, 2014; Zhang et al. 2008b). The mafic enclaves and their enclosing granitic gneisses are interpreted to be early Paleozoic high-grade metamorphic counterparts of the Meso-Neoproterozoic igneous protoliths, which were generated by magmatism during the development of the Rodinia supercontinent (e.g., Zhang et al. 2008b; Song et al. 2010, 2012; Xiong et al. 2012).

In the Shenglikou area (Fig. 1c), a rare outcrop (~500 m × 800 m) of garnet-facies peridotites (here named the "Shenglikou peridotite massif") is tectonically surrounded by felsic UHP gneisses. The gneissic foliation is almost parallel to the margin of the massif. Post-collisional S-type granites intruded the gneisses at 428–406 Ma (Wu et al. 2007). Quartz monzonite dykes crosscut the gneisses and penetrate into the Shenglikou peridotite massif. Cenozoic sediments transgress across the Qaidam block and unconformably overlie part of the gneiss and peridotite.

Sample descriptions

The Shenglikou peridotite massif is a composite (Fig. 1c), consisting of (1) major inner garnet-bearing peridotite zones rimmed by (2) garnet-free serpentinites of probably dunitic and harzburgitic origin and locally cross-cut by (3) later phlogopite-bearing garnet clinopyroxenite dykes [studied by Xiong et al. (2014)]. This study focuses on relatively fresh samples from part (1) and includes some serpentinites from part (2). We subdivided the studied samples into two groups: one rich in olivine (Ol) and the other rich in pyroxene (Pyro), with the boundary at a volume ratio of olivine/(olivine + clinopyroxene + orthopyroxene) of 70 %. The serpentinites are tentatively treated as belonging to the Ol-rich group, based on their refractory whole-rock major-element compositions (see results below), but we cannot exclude the possibility that their protolith had higher modes of Ca- and Al-rich minerals which have been destroyed during serpentinization.

The serpentinite zones are massive blocks or bands (Fig. 1c), with dark weathering surfaces and greenish-yellowish interiors (Online Resource 1). Oriented relics of pyroxene, olivine and spinel define a lineation parallel to the gneissosity of the wall rocks. Three representative serpentinites were used in this study (07SLK18, 07SLK35 and 09SLK01; Ol-rich group).

Blocks of garnet-bearing peridotite within the inner zone contain meter-to-centimeter layers of pyroxene-rich ultramafic rocks (sometimes grading to anhydrous clinopyroxenite). In some cases, such as sample 07SLK06 (Online Resource 1), the Pyro-rich (07SLK06L) and Ol-rich (07SLK06H) bands are thinly interlayered. Other representative samples from the Ol-rich group include 07SLK02 (Ol-rich lherzolite), 07SLK08 (Ol-rich lherzolite), 07SLK12 (harzburgite) and 07SLK29 (Ol-rich lherzolite);

those from the Pyro-rich group are 07SLK05 (clinopyroxenite) and 07SLK15 (Cpx-rich lherzolite; Cpx mode higher than 20 vol%). The point-counted mineral modes are given in Online Resource 2.

Olivine-rich group

Peridotites from the Ol-rich group have three modes of occurrence: (1) as serpentinites in the outer rim of the massif, (2) as large blocks in the interior of the massif and (3) as thin interlayers separated by Pyro-rich rocks. The serpentinites show a medium-grained texture, with a few relics of pyroxene, olivine and spinel embedded in the serpentinization products. Here, we mainly describe the Ol-rich blocks and interlayers, which both have porphyroblastic microstructures (Online Resource 1).

In blocks of the Ol-rich associations (dunite, harzburgite, lherzolite and wehrlite; depending on mineral modes; Online Resource 1), centimeter-size garnet, orthopyroxene and/or clinopyroxene are randomly embedded in a granoblastic, fine- to medium-grained matrix (Fig. 2a–f). The matrix is made up of olivine + orthopyroxene (Opx) + clinopyroxene (Cpx) + spinel (Sp) + amphibole (Amp) ± sulfide (Sulf) ± zircon and hydrous phases [e.g.,

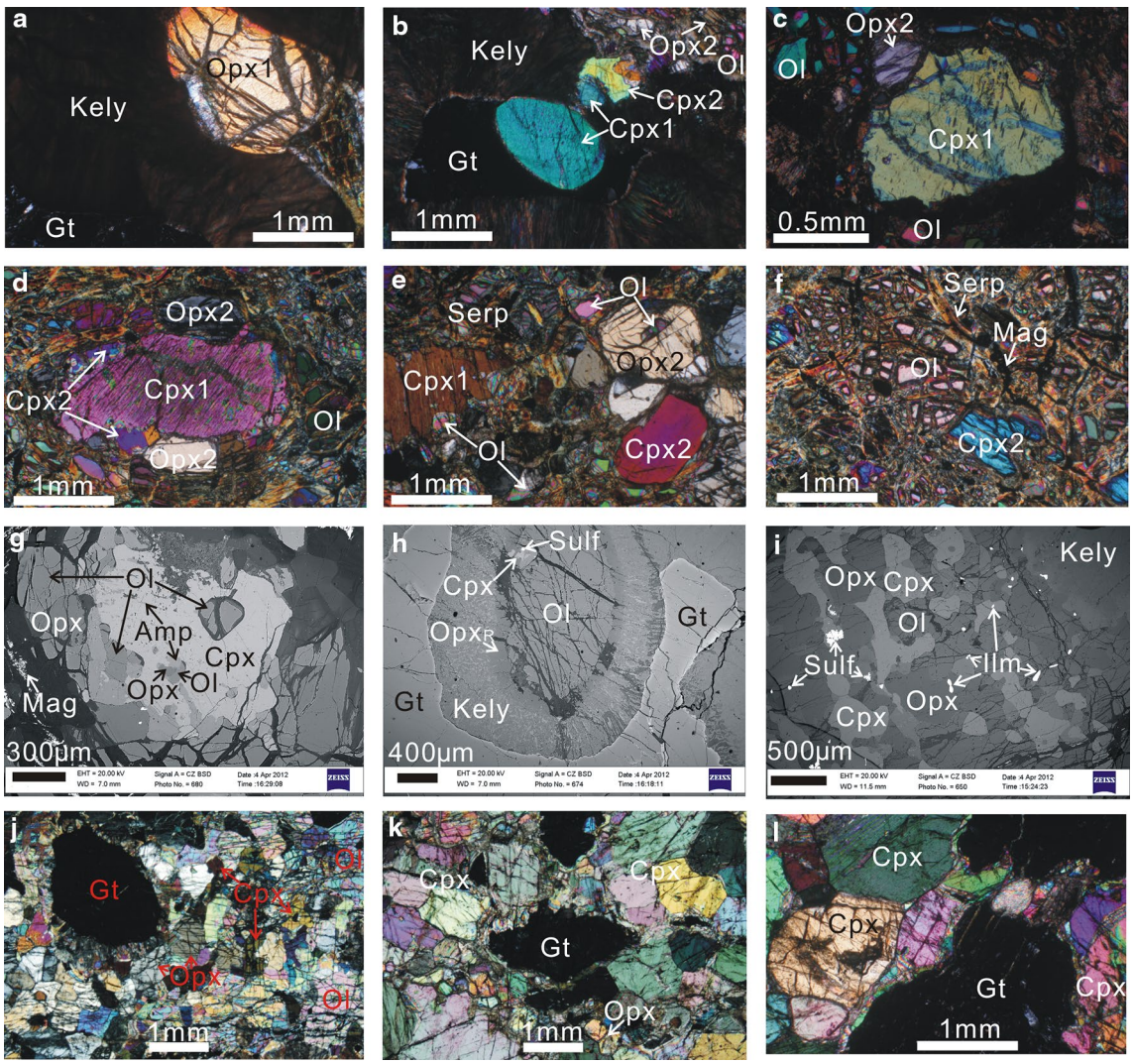

Fig. 2 Photomicrographs (crossed-polarized light, **a–f** and **j–l**; BSE, **g–i**) showing petrographic features and mineral assemblages of representative rock types in the Shenglikou peridotite massif. Ol-rich peridotite blocks are shown in **a–f**: **a–e** show the deformation features and relationships between porphyroblastic Gt, Opx1 and Cpx1 and the matrices of Cpx2, Opx2 and Ol; **f** shows the serpentine veins with the Ol and Cpx2 in the matrix. Ol-rich and Pyro-rich interlayers are exhibited in **g–l**: **g**, **h** show the Ca- and Al-rich minerals in the matrix of Ol and serpentinized products; **i**, **j** show Gt porphyroblasts set in a medium-grained matrix of two pyroxenes + Ol + Amp + Sp + Sulf + Ilm; (*k*, *l*) show the coarse-grained texture of clinopyroxenite interlayers (07SLK05). Mineral abbreviations: *Kely* kelyphite, *Gt* garnet, *Cpx* clinopyroxene, *Opx* orthopyroxene, *Ol* olivine, *Amp* amphibole, *Sp* spinel, *Sulf* sulfide, *Ilm* ilmenite, *Serp* serpentine, *Mag* magnetite

serpentine (Serp)]. The matrix grains closely surrounding the porphyroblasts show 120° triple junctions and a sheared microstructure and have localized more strain than the granular matrix domains away from the porphyroblasts (Fig. 2c–e). Garnet porphyroblasts contain exsolved needles of rutile (Ru) (Online Resource 3) and are surrounded by thick kelyphites of Sp + Cpx + Opx (Fig. 2a, b); sometimes pargasitic amphibole appears to rim the kelyphites. Ovoid porphyroblasts of Cpx and Opx occur within kelyphite/garnet or in the matrix (Fig. 2a–e). Cpx porphyroblasts usually host-oriented Fe–Cr oxides, serpentine, amphibole, apatite and phlogopite along the Cpx cleavages. Dense, thin and parallel lamellae of metal oxides and/or Cpx have exsolved from the Opx porphyroblasts. Rare ovoid, brown, medium-size grains of spinel are enclosed by completely kelyphitized garnet (Online Resource 3). Olivine in the matrix sometimes hosts rods or needles of ilmenite and Cr-spinel. Mesh-like serpentine encloses relict silicates in the matrix, and fine dark trails of magnetite outline the 120º triple junctions of former olivine grains (Fig. 2f). Veins of chrysotile and magnetite along cracks cut through the original lineation defined by porphyroblasts and the matrix minerals.

Interlayers of Ol-rich peridotites show stronger shearing and higher modes of garnet and pyroxene than those of the Ol-rich blocks. Garnet porphyroblasts and aggregates of pyroxene + amphibole + olivine form isolated "islands" within the matrix, which is dominated by olivine + serpentine (Fig. 2g). Lines of oriented magnetite and other deformed matrix minerals form a sheared array around these unserpentinized clusters. Garnet porphyroblasts have similar occurrence to those of olivine-rich blocks, but two differences are obvious: (1) They contain denser exsolution of rutile needles and inclusions of spinel, rutile and pyroxene; (2) the edges of garnet grains are embayed and tend to enclose recrystallized olivine porphyroblasts. There is a kelyphite layer near garnet and a recrystallized Opx rim around the recrystallized olivine (Fig. 2h). Medium-grained pyroxene and olivine have survived serpentinization and are in textural equilibrium with amphibole (Fig. 2g). These petrographic characteristics are similar to the interlayers in the Pyro-rich peridotites.

Pyroxene-rich group

Pyroxene-rich ultramafic rocks occur as layers within Ol-rich peridotites and show porphyroblastic (e.g., 07SLK06L, 07SLK15; Fig. 2i, j) and coarse-grained microstructures (e.g., 07SLK05; Fig. 2k, l).

In the Pyro-rich lherzolites (Online Resource 1), centimeter-size porphyroblasts of garnet, Cpx and Opx are set in a medium-grained matrix of Ol + Cpx + Opx + Amp + Sp + ilmenite (Ilm) + Sulf ± zircon. Garnet porphyroblasts show similarities to those in the Ol-rich interlayers, except that they contain more rutile needles. Cpx and Opx porphyroblasts are rare and display similar features to those in the Ol-rich blocks. The medium-sized Ol, Cpx, Opx and Amp in the matrix show textural equilibration. On the other hand, some vermicular grains of pyroxene and amphibole are distributed interstitially between euhedral or subhedral matrix silicates, and some amphiboles preserve relict textures from the amphibolitization of earlier Cpx. The preserved disequilibrium textures indicate the possible overprints of melt/fluid metasomatism. Fine-grained ilmenite, spinel and sulfide occur as either inclusions in anhydrous silicates or as interstitial phases between silicates (Online Resource 3). The melt-droplet shapes of these oxides and sulfides suggest an igneous origin, co-genetic with the anhydrous silicate matrix.

The Pyro-rich peridotites sometimes grade into layers of anhydrous clinopyroxenite (e.g., 07SLK05; Online Resource 1). Large garnet grains and medium-size pyroxenes are weakly deformed and oriented. Garnets (~20 vol%) have thin rims of kelyphite (Sp + Opx + Cpx ± Amp; Fig. 2k). Major Cpx (~75 vol%) shows 120° triple junctions with other silicates and encloses exsolved lamellae of Opx and Amp (Fig. 2l). Minor Opx (~3 vol%) is finer-grained. Rare spinel, ilmenite, sulfide and zircon are also found (in total <2 vol%). Locally, darker veins of recrystallized Cpx with abundant hydrous and opaque inclusions are parallel to the foliation of the rock. No major hydrous phases are found in equilibrium with garnet and pyroxene. The clinopyroxenite layers are thus different in this respect from the phlogopite-bearing pyroxenite dykes studied by Xiong et al. (2014).

Analytical methods

All methods, including analyses of whole-rock and mineral chemistry (Tables 1, 2; Online Resources 4 and 5) and Sr–Nd–Hf–Os–O isotopes (Tables 3, 4; Online Resources 6 and 7), have been described in the Online Resource 8.

Results

Whole-rock major- and trace-element compositions

Except for SiO_2, most of the oxides and trace elements (Tables 1, 2) of Shenglikou samples (from this study and literature) show little or no correlation with the degree of serpentinization (Online Resource 9). The negative Eu anomalies of three serpentinites from the Ol-rich group are inferred to be a secondary feature, the consequence of serpentinization or other unknown processes. The Mg# [molar $Mg^{2+}/(Mg^{2+}+Fe^{2+})$], magmaphile oxides (e.g., Al_2O_3) and moderately incompatible element contents (e.g., Yb)

Table 1 Major-element compositions (wt%) of whole rocks from the Shenglikou peridotite massif, North Qaidam (NE Tibet)

Sample ID	07SLK05[a]	07SLK06L[b]	07SLK15[b]	07SLK06H[b]	07SLK08[b]	07SLK18[b]	07SLK35[b]	09SLK01[b]
Lithology[c]	Gt-Pyrox	Gt-Lherz	Gt-Lherz	Gt-Harz	Gt-Lherz	Sp-Serp	Sp-Serp	Sp-Serp
Group[d]	Pyro-rich	Pyro-rich	Pyro-rich	Ol-rich	Ol-rich	Ol-rich	Ol-rich	Ol-rich
SiO_2	51.66	44.90	40.07	39.62	38.99	38.51	39.02	40.28
TiO_2	0.07	0.24	0.09	0.09	0.04	0.04	0.02	0.02
Al_2O_3	6.48	5.86	3.22	2.66	1.32	1.00	0.85	1.06
Cr_2O_3	0.46	n.a.	n.a.	n.a.	n.a.	n.a.	n.a.	n.a.
FeO_T	4.79	6.61	6.78	7.60	6.29	8.90	7.14	7.63
MnO	0.15	0.24	0.12	0.07	0.09	0.06	0.07	0.06
MgO	17.97	28.71	37.39	36.70	40.20	37.10	38.50	41.68
CaO	18.43	7.29	1.98	0.88	0.95	0.99	0.73	0.13
Na_2O	0.54	0.39	0.16	0.17	0.14	0.06	0.06	0.06
K_2O	0.00	0.03	0.02	0.03	0.03	0.01	0.00	0.01
P_2O_5	n.a.	0.01	0.01	0.01	0.01	0.01	0.01	0.01
LOI	n.a.	4.85	9.81	11.72	11.01	12.72	12.35	8.55
Total	100.54	99.13	99.65	99.55	99.07	99.40	98.75	99.49
Mg#	0.87	0.89	0.91	0.92	0.90	0.88	0.91	0.91

n.a. not analyzed

[a] Reconstructed data, using estimated mineral modes and EMP mineral data; [b]measured XRF data; [c]lithology includes Gt-bearing rocks of pyroxenite (Pyrox), lherzolite (Lherz) and harzburgite (Harz), and Gt-free/Sp-bearing serpentinite (Serp); [d]Group includes pyroxene-rich (Pyro-rich) ultramafic rocks and olivine-rich (Ol-rich) peridotites

mainly reflect the degree of melting, which controls the olivine proportions of the residual peridotites; this may also affect the degree of serpentinization (Online Resource 9). The other oxides and trace elements do not show any correlations with the LOI contents, suggesting that these elements are controlled by mantle processes that acted prior to serpentinization.

The major-element compositions of the Shenglikou Ol-rich and Pyro-rich ultramafic rocks show large ranges (Fig. 3), consistent with the variable mineral modes (Online Resources 1 and 2). The Ol-rich peridotites have similar FeO_T (10.27–7.14 wt%; Fig. 3a), higher MgO (45.83–41.80 wt%) and Mg# (0.919–0.881), but lower Al_2O_3 (3.04–0.98 wt%; Fig. 3b), CaO (1.14–0.14 wt%; Fig. 3c), TiO_2 (0.10–0.02 wt%; Fig. 3d) and Na_2O (0.20–0.07 wt%; Fig. 3e) relative to the Pyro-rich rocks. The interlayers of Pyro-rich lherzolite (07SLK06L) and clinopyroxenite (07SLK05) have major-element compositions more fertile than the primitive mantle (McDonough and Sun 1995).

The whole-rock trace-element compositions vary by more than one order of magnitude (Figs. 3f, 4). The concentrations of transition elements such as Sc (52–6.2 ppm), V (331–21 ppm), Cr (3164–2020 ppm), Co (110–35 ppm), Ni (2229–332 ppm), Cu (190–0.08 ppm) and Zn (56–15 ppm), are controlled by their compatibilities during melt-mineral partitioning and/or by the "nugget" effects of trace minerals (e.g., sulfide for Cu, and spinel for Cr, V and Zn). The lithophile elements with moderate incompatibility (e.g., Ga, Y and HREE) are negatively correlated with the depletion indicators (such as Al_2O_3 contents; Fig. 3f). All samples show enrichment in LREE, relative to MREE and HREE (Fig. 4a). The Ol-rich peridotites have lower REE contents than the Pyro-rich rocks and show gradual increases from Lu to La except 07SLK06H. The Pyro-rich rocks have "reversed spoon-shape" patterns, which show the greatest depletion at MREE. In a multi-element diagram (Fig. 4b) normalized to primitive-mantle values (McDonough and Sun 1995), both groups of rocks show general trends of enrichment from moderately to highly incompatible elements, and display strong positive anomalies of U, Pb and Li and negative anomalies of Nb, Zr, Hf and Ti (some samples), relative to their neighboring elements. The strong depletion of highly incompatible elements and HFSEs in the clinopyroxenite (07SLK05) probably reflects the fact that Ti- and volatile-rich micro-phases are not included in the whole-rock reconstruction.

Mineral major-element compositions

All the analyzed minerals other than medium-grained spinel are homogeneous in chemical compositions at the thick-section scale (Online Resource 4).

Table 2 Trace-element compositions (ppm) of whole rocks from the Shenglikou peridotite massif, North Qaidam (NE Tibet)

Sample ID	07SLK05	07SLK06L	07SLK15	07SLK06H	07SLK08	07SLK18	07SLK35	07SLK35	09SLK01
Lithology	Gt-Pyrox	Gt-Lherz	Gt-Lherz	Gt-Harz	Gt-Lherz	Sp-Serp	Sp-Serp	Sp-Serp	Sp-Serp
Group	Pyro-rich	Pyro-rich	Pyro-rich	Ol-rich	Ol-rich	Ol-rich	Ol-rich	Ol-rich	Ol-rich
Comments								Duplicate	
Li	1.98	11.4	2.98	5.00	2.31	3.15	1.67	1.57	1.75
Be	0.14	0.11	0.06	0.07	0.03	0.14	0.13	0.12	0.14
Sc	52.2	27.5	15.2	11.4	8.54	6.22	6.44	6.26	7.91
V	331	147	53.3	57.1	25.4	24.5	23.5	22.9	21.0
Cr	3164	2843	2680	2369	2020	2168	2250	2203	2203
Co	35.1	96.2	97.3	84.9	98.3	110	98.4	95.8	83.2
Ni	332	1227	1887	1923	2046	2229	2220	2166	2139
Cu	0.08	190	25.2	11.4	1.23	1.32	0.36	0.33	0.12
Zn	14.8	55.5	42.0	31.8	39.8	23.3	40.7	38.7	34.3
Ga	6.39	3.34	1.61	2.06	0.75	0.98	0.76	0.72	0.80
Rb	0.02	0.78	0.30	0.52	0.48	0.81	0.08	0.04	1.66
Sr	254	88.4	61.2	17.3	15.9	18.2	14.2	13.8	4.61
Y	5.40	5.41	2.61	2.05	0.70	0.76	0.72	0.71	1.02
Zr	9.57	7.61	3.59	4.06	3.14	1.52	0.43	0.41	0.76
Nb	0.01	1.52	2.30	0.57	0.87	0.41	0.17	0.17	0.26
Cs	0.02	0.58	0.06	0.22	0.08	0.10	0.01	0.01	0.36
Ba	0.02	15.2	17.4	11.5	13.8	1.51	4.06	3.96	12.7
La	5.46	1.87	0.84	0.97	0.43	0.34	0.60	0.58	0.24
Ce	23.1	6.02	2.01	3.00	1.13	0.99	1.40	1.39	0.61
Pr	3.61	0.95	0.24	0.45	0.18	0.14	0.17	0.16	0.10
Nd	15.0	4.02	0.97	1.86	0.88	0.58	0.71	0.66	0.44
Sm	2.30	0.58	0.22	0.31	0.20	0.12	0.14	0.14	0.15
Eu	0.58	0.17	0.07	0.09	0.05	0.01	0.01	0.01	0.01
Gd	1.29	0.61	0.27	0.24	0.15	0.13	0.14	0.12	0.20
Tb	0.16	0.11	0.05	0.04	0.02	0.02	0.02	0.02	0.03
Dy	0.97	0.76	0.37	0.29	0.10	0.12	0.12	0.11	0.17
Ho	0.22	0.20	0.09	0.08	0.03	0.03	0.03	0.02	0.03
Er	0.66	0.66	0.29	0.24	0.09	0.07	0.07	0.08	0.08
Tm	0.11	0.11	0.06	0.04	0.02	0.02	0.01	0.01	0.02
Yb	0.83	0.75	0.33	0.27	0.12	0.11	0.09	0.08	0.10
Lu	0.14	0.13	0.06	0.04	0.02	0.02	0.01	0.01	0.02
Hf	0.50	0.29	0.12	0.15	0.13	0.06	0.02	0.02	0.02
Ta	0.00	0.15	0.12	0.05	0.07	0.03	0.02	0.02	0.03
Pb	13.8	6.71	2.30	1.96	0.70	0.31	0.33	0.25	0.26
Th	0.14	0.08	0.05	0.05	0.02	0.05	0.09	0.09	0.26
U	0.04	0.15	0.19	0.05	0.01	0.12	0.51	0.49	0.09

Trace-element data of 07SLK25 come from the reconstruction using estimated mineral modes and LA-ICPMS data; the other samples are analyzed by ICPMS; lithology and group are as same as the footnotes of Table 1

Garnet

Garnets (Online Resource 4) in the Ol-rich group are composed mainly of pyrope (~73–71 %), almandine (~16–10 %), grossular (~6–4 %) and uvarovite (~8–6 %) with lesser proportions of spessartine (≤1 %), while garnets in the Pyro-rich group have lower contents of pyrope (~72–64 %) and uvarovite (~6–1 %), higher contents of almandine (~22–13 %), and similar proportions of grossular and spessartine. The CaO contents (Fig. 5a) and Mg# (Fig. 5b) of the garnets in the two groups are both positively correlated with Cr_2O_3 contents. Garnets in the Ol-rich group

Table 3 In situ Re–Os isotopic data of sulfides from the Shenglikou peridotite massif, North Qaidam (NE Tibet)

Sample ID		07SLK15@04	07SLK15@12	07SLK15@16	07SLK06L@07	07SLK06L@08
$^{187}Re/^{188}Os$		0.875	0.394	0.664	0.646	0.530
1σ		0.094	0.002	0.033	0.010	0.061
$^{187}Os/^{188}Os$		0.1138	0.1066	0.1496	0.1207	0.1202
1σ		0.0043	0.0006	0.0072	0.0019	0.0130
$^{187}Os/^{188}Os_I$	$t = 0.43$ Ga	0.1075	0.1037	0.1448	0.1160	0.1164
1σ		0.0044	0.0006	0.0072	0.0019	0.0130
T_{MA} (ECR)	(Ga)	−1.9	35.7	5.1	−2.0	−4.5
1σ	(Ga)	0.7	2.3	1.8	0.5	8.2
T_{RD} (ECR)	(Ga)	2.0	3.0	n.a.	1.0	1.1
1σ	(Ga)	0.6	0.1	1.1	0.3	1.8
T_{MA} (CHUR)	(Ga)	−1.7	79.5	5.0	−1.6	−3.3
T_{RD} (CHUR)	(Ga)	1.9	3.0	n.a.	0.9	1.0
T_{MA} (PUM)	(Ga)	−2.2	27.2	5.0	−2.6	−6.3
T_{RD} (PUM)	(Ga)	2.1	3.1	n.a.	1.2	1.3

^{187} $Os/^{188}Os_I$, initial $^{187}Os/^{188}Os$ ratios calculated back to 0.43 Ga; T_{MA}, model ages calculated using measured $^{187}Re/^{188}Os$ and $^{187}Os/^{188}Os$ ratios, as suggested by Shirey and Walker (1998); T_{RD}, Re-depleted model ages calculated using the way suggested by Shirey and Walker (1998); model ages based on enstatite chondrite reservoir (ECR; Walker et al. 2002), chondritic uniform reservoir (CHUR; Shirey and Walker 1998) and primitive upper mantle (PUM; Meisel et al. 2001)."n.a." means negative T_{RD} values

have higher Cr_2O_3 (2.89–1.62 wt%), CaO (5.43–4.43 wt%) and Mg# (0.84–0.77) than those of Pyro-rich group.

Spinel

Spinels (Online Resource 4) from the two groups occur as either primary fine-medium grains or secondary vermicular veins within kelyphites. The secondary spinels have lower Cr# [0.17–0.04; molar $Cr^{3+}/(Cr^{3+}+Al^{3+})$; Fig. 5c] and TiO_2 ($\leq$0.03 wt%; Fig. 5d) and higher Mg# (0.86–0.69) and NiO (0.35–0.05 wt%) than those of the cores of primary grains. Two grains from 07SLK02 have recrystallized rims (Online Resource 3), showing lower Cr# and higher Mg# than the cores. Among the primary grains, a spinel from the Pyro-rich interlayer (07SLK06L) gives the lowest Cr# of 0.48 and the highest Mg# of 0.59 and TiO_2 (0.72 wt%); the other spinels from Ol-rich peridotites have Cr# (up to 0.71), Mg# (down to 0.37) and TiO_2 (0.61–0.03 wt%), similar to the compositions of spinels from forearc peridotites (Arai and Ishimaru 2008).

Olivine

Olivine grains (Online Resource 4) occur as primary phases in the matrix and secondary ones enclosed by Opx rims (Fig. 2h). Among the primary olivines, grains from Ol-rich blocks have higher Mg# (0.92–0.91), NiO (0.49–0.35 wt%) and lower MnO (0.17–0.09 wt%), compared to grains from Ol-rich interlayers and Pyro-rich peridotites (Fig. 5e, f). The secondary olivines show even lower Mg# (down to 0.86) but have higher NiO (up to 0.81 wt%) and MnO (up to 0.40 wt%) than the primary ones.

Clinopyroxene

Clinopyroxenes from the two groups are all diopsidic (Online Resource 4). Clinopyroxenes from Ol-rich peridotites have higher contents of Cr_2O_3 (1.89–0.96 wt%), Al_2O_3 (2.67–1.27 wt%), Na_2O (1.90–0.43 wt%) and higher Mg# (0.96–0.94) than those of Pyro-rich rocks (Fig. 6a, b). Clinopyroxenes show similar compositions in the interlayers of Pyro-rich (07SLK06L) and Ol-rich peridotites (07SLK06H), but an inclusion within olivine from 07SLK06H gives the highest Al_2O_3 content of 3.18 wt%. The clinopyroxenes from the clinopyroxenite interlayer (07SLK05) have the lowest Mg# and Cr_2O_3 contents among all samples.

Orthopyroxene

Compared to the secondary grains (Online Resource 4), primary orthopyroxenes occurring as porphyroblasts or in the matrix have higher Mg# (up to 0.93; Fig. 6c, d) and Cr_2O_3 (up to 0.68 wt%), lower Al_2O_3 (down to 0.33 wt%) and similar CaO contents. Orthopyroxenes from the Ol-rich peridotites generally have higher Mg# and Cr_2O_3 but lower Al_2O_3 contents than those in the Pyro-rich group.

Amphibole, ilmenite and rutile

Amphiboles from the two groups are all magnesiohornblende (Online Resource 4). The amphiboles found as medium-sized grains in the matrix or as exsolutions/inclusions within clinopyroxene have higher Mg#, TiO_2 (up to

Table 4 Sr–Nd–Hf isotopic data of minerals and whole rocks from the Shenglikou peridotite massif, North Qaidam (NE Tibet)

Sample ID	07SLK06L	07SLK06L	07SLK06L	07SLK06L	07SLK06H	07SLK06H
Target	Cpx	Gt	Amp	WR	Cpx	Gt
$^{87}Rb/^{86}Sr$	0.001426	0.902668	0.060191	0.008791	0.001977	0.593334
1σ	0.000549	0.051149	0.001190	0.000614	0.000633	0.030473
$^{87}Sr/^{86}Sr$	0.707679	0.711180	0.707633	0.707674	0.707640	0.707209
1σ	0.000002	0.000006	0.000003	0.000002	0.000003	0.000012
$^{87}Sr/^{86}Sr_I$	0.707670	0.705651	0.707265	0.707620	0.707627	0.703575
1σ	0.000004	0.000313	0.000008	0.000004	0.000005	0.000187
ε_{Sr} (t)	52.2	23.6	46.5	51.5	51.6	−6.0
1σ	0.1	4.5	0.1	0.1	0.1	2.7
T_{CHUR} (Ma)	−2810	571	−10556	−3091	−2794	373
1σ	19	36	602	26	22	22
$^{147}Sm/^{144}Nd$	0.082789	0.523520	0.080450	0.095673	0.085839	0.434868
1σ	0.002822	0.023100	0.003095	0.003382	0.004204	0.021304
$^{143}Nd/^{144}Nd$	0.511916	0.513674	0.511921	0.511970	0.511929	0.513205
1σ	0.000003	0.000037	0.000015	0.000003	0.000008	0.000010
$^{143}Nd/^{144}Nd_I$	0.511682	0.512200	0.511695	0.511700	0.511687	0.511980
1σ	0.000008	0.000075	0.000017	0.000010	0.000014	0.000061
ε_{Nd} (t)	−7.7	2.4	−7.5	−7.4	−7.6	−1.9
1σ	0.2	1.5	0.3	0.2	0.3	1.2
T_{DM} (Ma)	1437	258	1405	1523	1455	38
1σ	31	26	37	44	49	8
T_{CHUR} (Ma)	962	487	935	1003	970	367
1σ	24	38	32	34	39	33
$^{176}Lu/^{177}Hf$	0.004496	0.634774	0.006621	0.097860	0.004715	0.397378
1σ	0.000981	0.028900	0.000611	0.004705	0.001746	0.019401
$^{176}Hf/^{177}Hf$	0.282600	0.290985	0.282881	0.283902	0.282634	0.288057
1σ	0.000010	0.000023	0.000034	0.000010	0.000028	0.000119
$^{176}Hf/^{177}Hf_I$	0.282564	0.285874	0.282827	0.283114	0.282596	0.284857
1σ	0.000013	0.000234	0.000034	0.000039	0.000031	0.000196
ε_{Hf} (t)	1.7	118.9	11.1	21.2	2.9	82.9
1σ	0.5	8.3	1.2	1.4	1.1	7.0
T_{DM} (Ma)	1020	691	621	584	973	713
1σ	33	33	58	47	66	42
T_{CHUR} (Ma)	340	726	−190	924	280	771
1σ	22	35	68	68	54	44

Sample ID	07SLK06H	07SLK06H	07SLK12	07SLK12	07SLK12
Target	Amp	WR	Cpx	Gt	WR
$^{87}Rb/^{86}Sr$	0.050153	0.011246	0.000413	0.738341	0.000713
1σ	0.000859	0.000671	0.000196	0.052212	0.000220
$^{87}Sr/^{86}Sr$	0.709037	0.707901	0.705600	0.711446	0.705602
1σ	0.000002	0.000003	0.000003	0.000017	0.000003
$^{87}Sr/^{86}Sr_I$	0.708730	0.707832	0.705597	0.706924	0.705598
1σ	0.000006	0.000005	0.000003	0.000320	0.000003
ε_{Sr} (t)	67.3	54.5	22.8	41.6	22.8
1σ	0.1	0.1	0.0	4.5	0.0
T_{CHUR} (Ma)	−10,572	−3434	−948	742	−953
1σ	301	33	3	59	4
$^{147}Sm/^{144}Nd$	0.079472	0.104057	0.092893	0.589087	0.117473

Table 4 continued

Sample ID	07SLK06H	07SLK06H	07SLK12	07SLK12	07SLK12
Target	Amp	WR	Cpx	Gt	WR
1σ	0.002294	0.004518	0.004740	0.014634	0.005224
$^{143}Nd/^{144}Nd$	0.511932	0.512003	0.512194	0.514195	0.512293
1σ	0.000011	0.000008	0.000006	0.000004	0.000006
$^{143}Nd/^{144}Nd_I$	0.511708	0.511710	0.511933	0.512536	0.511963
1σ	0.000012	0.000015	0.000015	0.000041	0.000016
ε_{Nd} (t)	−7.2	−7.2	−2.8	8.9	−2.3
1σ	0.2	0.3	0.3	0.8	0.3
T_{DM} (Ma)	1383	1593	1206	425	1357
1σ	26	66	48	17	74
T_{CHUR} (Ma)	914	1039	645	607	654
1σ	23	53	31	23	45
$^{176}Lu/^{177}Hf$	0.007296	0.082469	0.000404	0.135129	0.025282
1σ	0.000492	0.004371	0.000146	0.003324	0.000881
$^{176}Hf/^{177}Hf$	0.282844	0.283766	0.282293	0.286023	0.282982
1σ	0.000017	0.000028	0.000009	0.000007	0.000028
$^{176}Hf/^{177}Hf_I$	0.282785	0.283102	0.282289	0.284935	0.282778
1σ	0.000018	0.000045	0.000009	0.000028	0.000028
ε_{Hf} (t)	9.6	20.8	−8.0	85.7	9.3
1σ	0.6	1.6	0.3	1.0	1.0
T_{DM} (Ma)	697	623	1336	1515	1090
1σ	32	70	13	51	132
T_{CHUR} (Ma)	−121	1066	789	1683	−1282
1σ	36	99	14	54	228

$^{87}Sr/^{86}Sr_I$, $^{143}Nd/^{144}Nd_I$ and $^{176}Hf/^{177}Hf_I$ are initial Sr–Nd–Hf isotopic ratios calculated back to 430 Ma; T_{CHUR}, CHUR model ages; T_{DM}, depleted-mantle model ages; whole-rock (WR) data are reconstructed by the estimated mineral mass fractions and analyzed mineral isotopic ratios, the Gt, Cpx and Amp contribute most of the Rb–Sr, Sm–Nd and Lu–Hf in the whole-rock systems (Online Resource 8). Decay constants: $\lambda_{Rb} = 1.42 \times 10^{-11}$ a^{-1} (Steiger and Jäger 1977), $\lambda_{Sm} = 6.54 \times 10^{-12}$ a^{-1} (DePaolo 1981) and $\lambda_{Lu} = 1.865 \times 10^{-11}$ a^{-1} (Scherer et al. 2001). Present-day CHUR: $^{87}Rb/^{86}Sr = 0.0827$, $^{87}Sr/^{86}Sr = 0.7045$ (Zindler and Hart 1986); $^{147}Sm/^{144}Nd = 0.1960$, $^{143}Nd/^{144}Nd = 0.512630$, $^{176}Lu/^{177}Hf = 0.0336$, $^{176}Hf/^{177}Hf = 0.282785$ (Bouvier et al. 2008). Present-day DM: $^{147}Sm/^{144}Nd = 0.21357$, $^{143}Nd/^{144}Nd = 0.51315$ (DePaolo 1981); $^{176}Lu/^{177}Hf = 0.0384$, $^{176}Hf/^{177}Hf = 0.283251$ (Griffin et al. 2000)

1.17 wt%) and Cr_2O_3 (up to 2.28 wt%) than those of secondary amphiboles that occur within kelyphites or as overgrown rims (Fig. 6e, f).

Ilmenite grains have TiO_2 of 57.4–55.1 wt %, FeO of 38.9–30.5 wt % and MgO of 11.4–5.0 wt% (Online Resource 4), similar to the compositions of ilmenites from kimberlites (e.g., Haggerty and Tompkins 1983). Two small grains of rutile included in garnets from 07SLK06L have ~98 wt% TiO_2 and low contents of SiO_2, Cr_2O_3, FeO and CaO (Online Resource 4).

Mineral trace-element compositions

Garnet

LA-ICPMS data (Online Resource 5) for garnet show small variations within each sample. Garnets from the Pyro-rich group and the remnant islands in 07SLK06H exhibit gradual enrichment from LREE to HREE (Fig. 7a); those from the Ol-rich blocks display steep increases from La to Sm and then slow decreases from Sm to Tb, followed by more gradual increases from Tb to Lu. In a multi-element diagram (Fig. 7b) normalized to the primitive-mantle composition, all garnets show strong negative anomalies of Ba, La, Sr, Ti and Li relative to neighboring elements and display different extents of enrichment or fractionation of HFSEs.

Clinopyroxene and amphibole

Clinopyroxene and amphibole are the two major reservoirs for incompatible lithophile elements in the whole-rock samples (Online Resources 5, 10), and their similar trace-element patterns mimic those of whole rocks. Clinopyroxenes from both groups show gradual depletions from LREE to HREE (Fig. 7c). Clinopyroxenes in 07SLK29 (Ol-rich

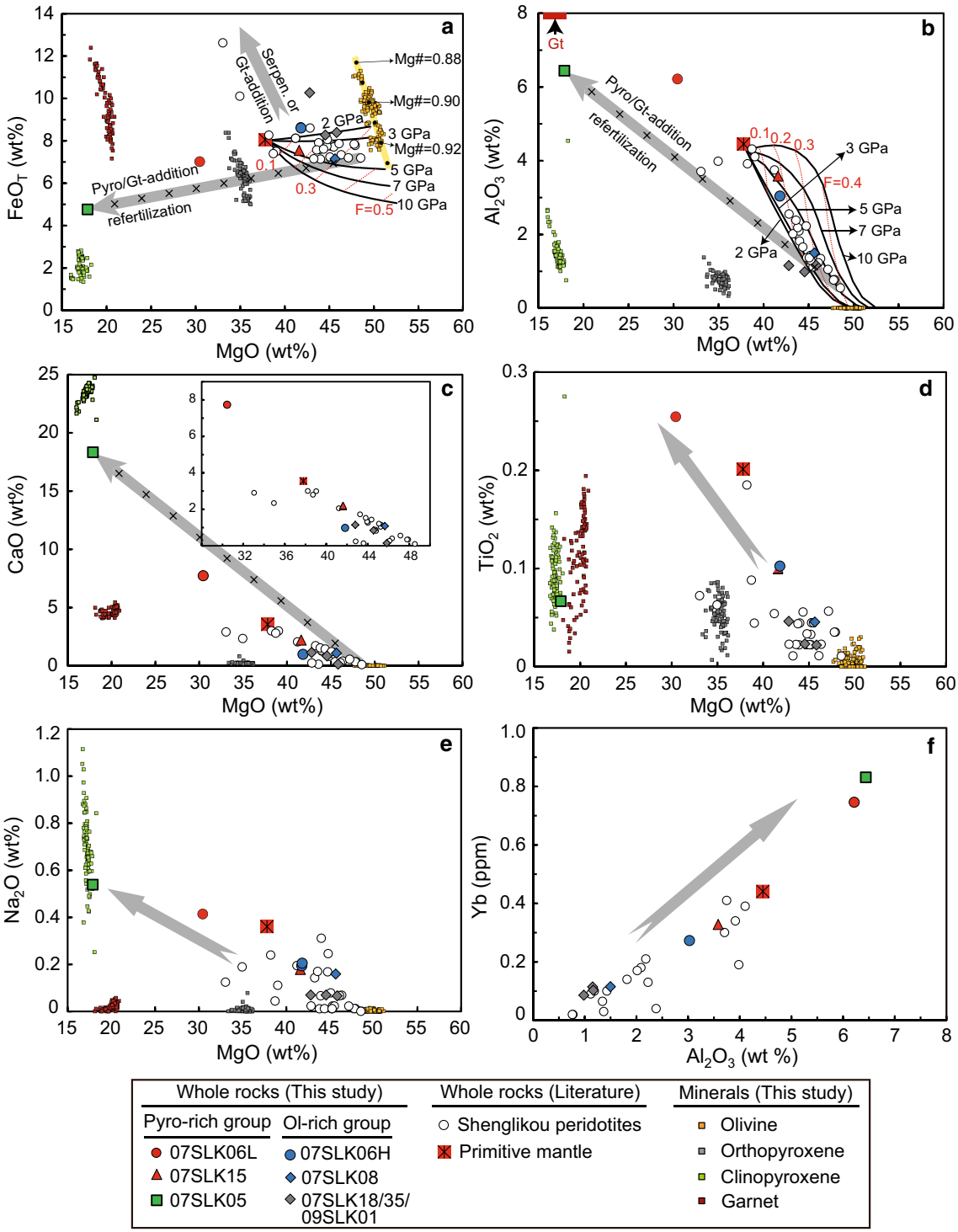

Fig. 3 Variations of MgO versus FeO_T (**a**), Al_2O_3 (**b**), CaO (**c**), TiO_2 (**d**) and Na_2O (**e**), and of Al_2O_3 versus Y (**f**) of representative whole rocks from the Shenglikou peridotite massif. Mineral compositions from this study are also plotted to show the effect of mantle refertilization. Literature whole-rock data are from Song et al. (2007), Yang and Powell (2008) and Shi et al. (2010); primitive-mantle compositions come from McDonough and Sun (1995). In (**a**, **b**), compositional contours of the melting residual peridotites are modeled as *thick black curves*, using the method of Herzberg (2004); the pressures (2, 3, 5, 7 and 10 GPa) represent the starting pressures of the fractional melting under adiabatic decompression, from a primitive-mantle protolith; the *red dashed curves* mark the degrees of melt extraction, as shown by the *red numbers* $F = 0.1$–0.5. The *thick yellow line* with *black dots* shows the olivine compositions with Mg# of 0.88–0.93. The *gray arrows* in (**a**–**f**) point to possible trends of refertilization by silicate melts, based on a refractory peridotitic protolith; *gray arrows* marked with black crosses in (**a**–**c**) show the two-endmember mixing results: pyroxenite (07SLK05) as one endmember, while the most depleted dunite (92SLK202; Yang and Powell 2008) as the other endmember

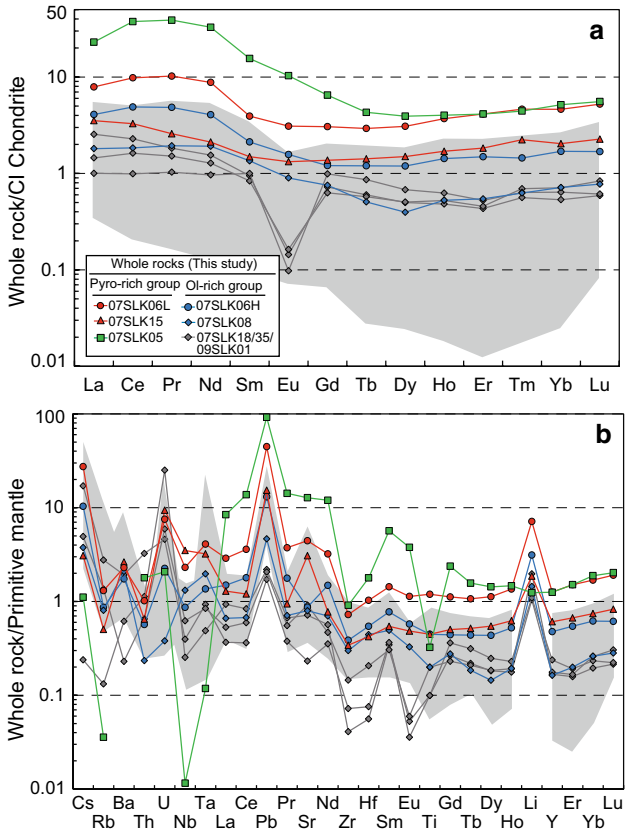

Fig. 4 REE (**a**) and multi-element (**b**) patterns of representative whole rocks in the Shenglikou peridotite massif, normalized to the values for chondrites and the primitive mantle (McDonough and Sun 1995), respectively. *Gray regions* represent the Shenglikou whole-rock trace-element data from the literature (Song et al. 2007; Shi et al. 2010)

block) and 07SLK05 (Pyro-rich interlayer) exhibit the strongest enrichment of LREE and the strongest depletion of HREE, and those of 07SLK06H and 07SLK06L are very similar, possibly indicating a similar origin. In a primitive-mantle normalized diagram (Fig. 7d), clinopyroxenes in Pyro-rich rocks have strong depletion of HFSE and obvious positive anomalies of Pb and Li, while those of Ol-rich peridotites show relatively higher abundances of highly incompatible elements and Li.

Amphiboles were analyzed only from the interlayers of 07SLK06H and 07SLK06L; their REE (Fig. 7e) and multi-element patterns (Fig. 7f) are very similar, as are those of clinopyroxenes from the two samples. They have strong positive anomalies of Pb and Li relative to REEs, but small depletions in Th, Ta and Zr compared to neighboring elements.

Orthopyroxene and olivine

Orthopyroxene and olivine are poor reservoirs for lithophile elements in the whole-rock samples (Online Resources 5, 10). Orthopyroxene displays large variations in highly incompatible elements and strong positive anomalies of Pb, Ti and Li (Online Resource 11), while olivine shows marked positive anomalies in fluid-mobile elements (U, Pb and Li), relative to neighboring elements. The abundances of other lithophile elements in orthopyroxene and olivine are usually about 0.1–0.01 times the values of primitive mantle.

P–T estimates

The Al-in-Opx barometers of Nickel and Green (1985) (P_{NG85}) and Brey and Kohler (1990) (P_{BK90}) were applied to the pressure estimation using EMP data for garnet and orthopyroxene in microstructural equilibrium (Online Resource 12). We used thermometers based on Fe–Mg exchange between two pyroxenes (T_{W77}, Wells 1977), garnet–olivine ($T_{O'NW79}$, O'Neill and Wood 1979) and garnet–clinopyroxene (T_{EG79}, Ellis and Green 1979; T_{B95}, Berman et al. 1995), and also used the Ca-in-Opx thermometer (T_{BKCa90}, Brey and Kohler 1990). The peak assemblages of minerals (stages 1 and 2; see footnotes of Online Resource 12) in the Pyro-rich group give similar *P–T* estimates (P = ~3.3–2.8 GPa, T = ~846–761 °C; Fig. 8). Porphyroblastic pairs in the Ol-rich peridotites yield higher *P–T* estimates than those in Pyro-rich rocks (up to 5.5 GPa and 1057 °C).

Sulfide Re–Os isotopes

Out of ~170 analyses of sulfides from the Shenglikou peridotite massif, only five grains give acceptable Re–Os isotopic data [relatively high Os intensity (0.0014–0.0110 V total Os) and $^{187}Re/^{188}Os < 1.0$; Table 3]. The five analyses were all acquired on sulfides in the Pyro-rich peridotites (three from 07SLK15, two from 07SLK06L). Measured $^{187}Re/^{188}Os$ and $^{187}Os/^{188}Os$ ratios vary from 0.875 to 0.394 and from 0.1496 to 0.1066 (Fig. 9), respectively. The initial $^{187}Os/^{188}Os$ ratios calculated back to 430 Ma range from 0.1448 to 0.1037 and give model ages (T_{RD} of 3.0–1.0 Ga) by reference to the ECR reservoir (Walker et al. 2002).

Sr–Nd–Hf isotopes of minerals and reconstructed whole rocks

In situ Rb–Sr isotopes

Rb–Sr isotopes were acquired in situ on clinopyroxenes and amphiboles from 07SLK06L and 07SLK06H (Online Resource 6). Ten analyses of clinopyroxenes give measured $^{87}Rb/^{86}Sr$ (0.04004–0.00021) and $^{87}Sr/^{86}Sr$ (0.70810–0.70596), with initial $^{87}Sr/^{86}Sr$ ratios of 0.70808–0.70596 at 430 Ma. Six results from amphibole show higher $^{87}Rb/^{86}Sr$

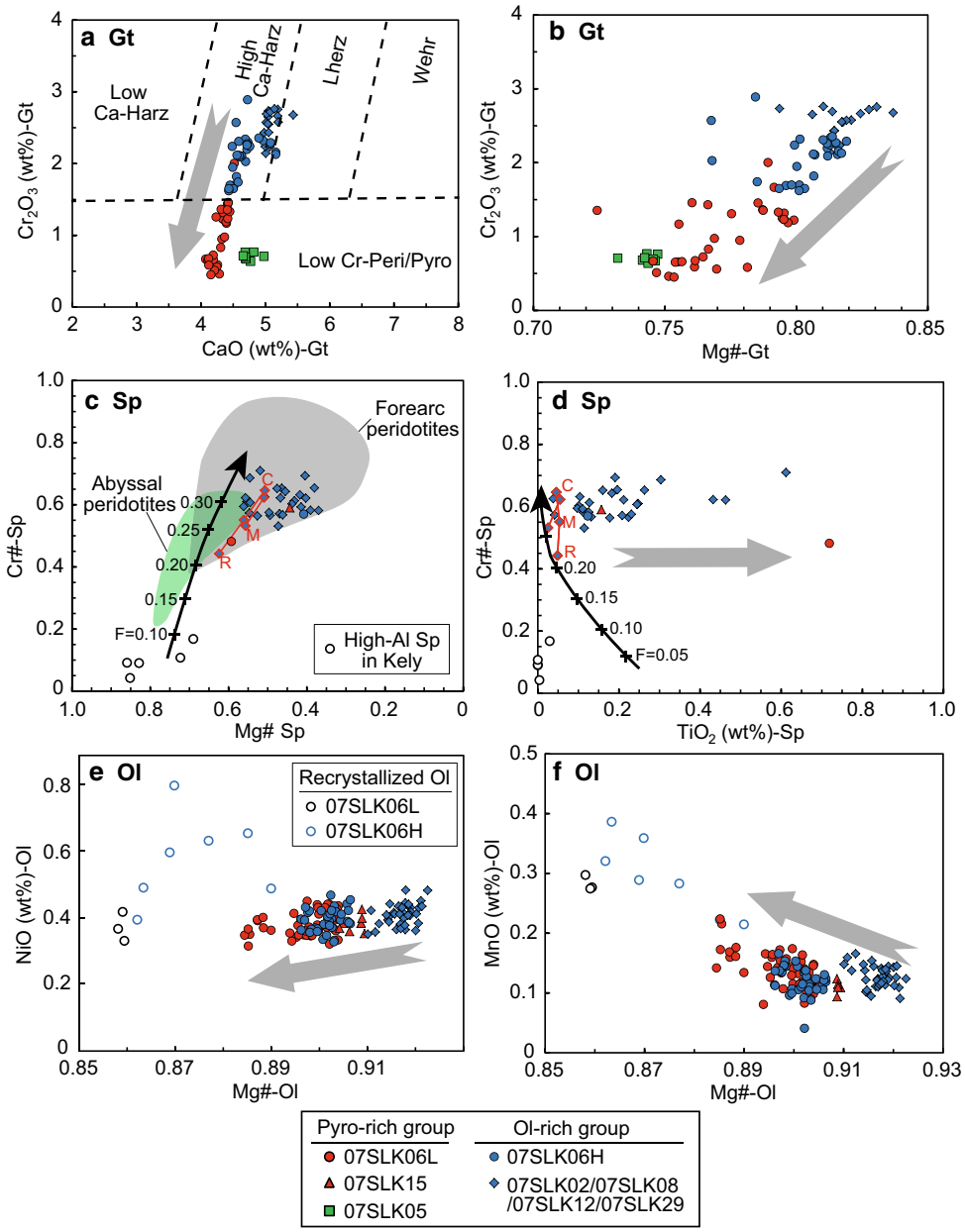

Fig. 5 Variations of CaO versus Cr_2O_3 (**a**; *garnet*), Mg# versus Cr_2O_3 (**b**; *garnet*), Mg# versus Cr# (**c**; *spinel*), TiO_2 versus Cr# (**d**; *spinel*), Mg# versus NiO (**e**; *olivine*) and Mg# versus MnO (**f**; *olivine*) for minerals in the Shenglikou peridotite massif. The *gray arrows* suggest refertilization trends. The *dashed lines* in (**a**) mark the garnet fields that correspond to different ultramafic hosts (Griffin et al. 2002b). The *thick, black curves* with *arrows* in **c**, **d** show the fractional melting trends of spinel and melting degrees (F) in the residual peridotite, using the modeling method of Pearce et al. (2000). The *green and gray regions* in **c** are from the collections of Dick and Bullen (1984) and Arai and Ishimaru (2008), respectively. The red "C, M and R" connected by *red lines* represent the core, mantle and rim compositions of each individual spinel

(0.08208–0.03864), but similar $^{87}Sr/^{86}Sr$ (0.70931–0.70731) and $^{87}Sr/^{86}Sr_I$ (0.70886–0.70707), compared to those of clinopyroxenes.

Sr–Nd–Hf isotopes by solution

Sr–Nd–Hf isotopes of garnet, clinopyroxene and amphibole separated from representative peridotites [Pyro-rich interlayer (07SLK06L), Ol-rich interlayer (07SLK06H) and Ol-rich block (07SLK12)] also were analyzed (Table 4). The whole-rock isotopic ratios were reconstructed using the estimated mass fractions of minerals and the measured compositions of relevant elements and isotopic ratios (Online Resource 10).

Minerals and whole rocks of the three samples show similar $^{87}Sr/^{86}Sr_I$ ratios (0.70873–0.70358), largely consistent with those analyzed by in situ method (Online Resource 13).

Garnets have higher $^{147}Sm/^{144}Nd$ (0.58909–0.43487), $^{143}Nd/^{144}Nd$ (0.514120-0.51321) and $^{143}Nd/^{144}Nd_I$ (0.51254–0.51198) than those of clinopyroxenes, amphiboles and whole rocks. The clinopyroxenes, amphiboles and whole rocks have similar Sm–Nd isotopic compositions (Online Resource 13): low $^{143}Nd/^{144}Nd_I$ (0.51196–0.51168), negative $\varepsilon_{Nd}(t = 430\ Ma)$ (−1.9 to −7.7), and Proterozoic T_{DM} (1.6–1.2 Ga) and T_{CHUR} ages (1.0–0.6 Ga).

All samples show larger variations in Lu–Hf isotopes than in Sm–Nd isotopes. The $\varepsilon_{Hf}(t = 430\ Ma)$ values of

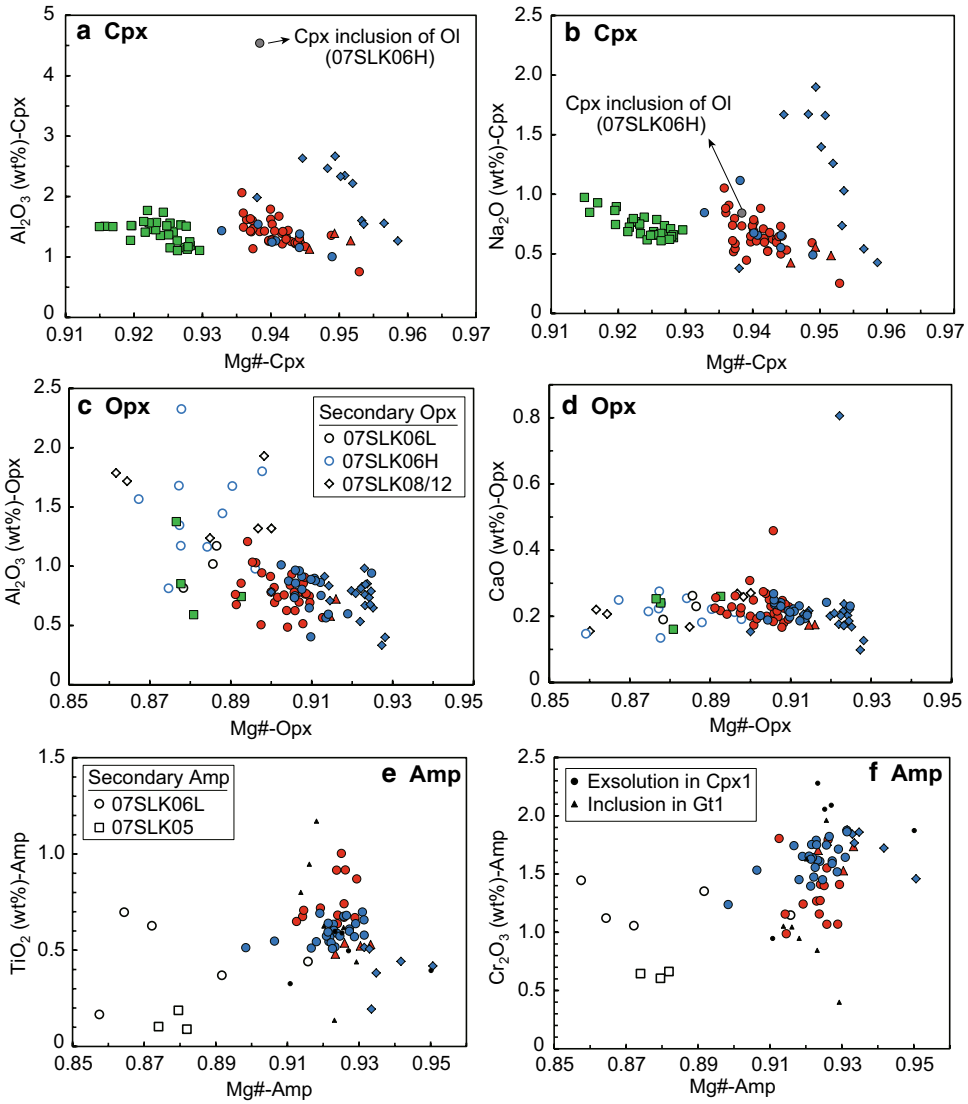

Fig. 6 Variations of Mg# versus Al_2O_3 (**a**; *clinopyroxene*), Na_2O (**b**; *clinopyroxene*), Al_2O_3 (**c**; *orthopyroxene*), CaO (**d**; *orthopyroxene*), TiO_2 (**e**; *amphibole*) and Cr_2O_3 (**f**; *amphibole*) for minerals in the Shenglikou peridotite massif. Other sample legends are the same as in Fig. 5

garnet, clinopyroxene, amphibole and whole rock vary from 118 to 82, 2.9 to −8.0, 11.1–9.6 and 21.2–9.3, respectively. In the Pyro-rich and Ol-rich interlayers (07SLK06L and 07SLK06H), clinopyroxenes have similar T_{DM} ages (1020 Ma versus 973 Ma), consistent with zircon T_{DM} ages (Xiong et al. 2011), while those of garnet, amphibole and whole rocks range from 713 to 584 Ma. Clinopyroxene and garnet in the Ol-rich block (07SLK12) yield T_{DM} ages that are undistinguishable within error (1336 Ma versus 1515 Ma). Hf T_{CHUR} ages range from 1683 Ma to future.

The calculated Sm–Nd isochron ages vary from 615 ± 37 Ma to 548 ± 65 Ma (Fig. 10a). Lu–Hf isochrons (Fig. 10b) defined by minerals in the Pyro-rich and Ol-rich interlayers (07SLK06L and 07SLK06H) show similar ages of 696 ± 140 Ma and 721 ± 170 Ma, consistent with the Hf T_{DM} ages of garnet, amphibole and whole rock. In the Ol-rich block (07SLK12), garnet and clinopyroxene give an isochron age of 1465 ± 65 Ma, which is similar to the Hf T_{DM} ages of minerals. The isochron ages and Lu–Hf isotopic equilibration are also modeled in Fig. 11, and the similar modeling for the Sm–Nd system is shown in Online Resource 14.

Oxygen isotopes of zircon and garnet

$\delta^{18}O$ values (Online Resource 7) of zircon from 07SLK02 (Ol-rich block) vary from 6.12 to 5.51 ‰, with a weighted average of 5.83 ± 0.08 ‰ ($n = 20$, 2σ, MSWD = 1.3); those of zircon from the clinopyroxenite interlayer (07SLK05) range from 6.13 to 5.70 ‰, with a weighted average of 5.97 ± 0.09 ‰ ($n = 14$, 2σ, MSWD = 0.95). The U–Pb ages, trace-element and Lu–Hf-isotope compositions of the zircons have been reported by Xiong et al. (2011).

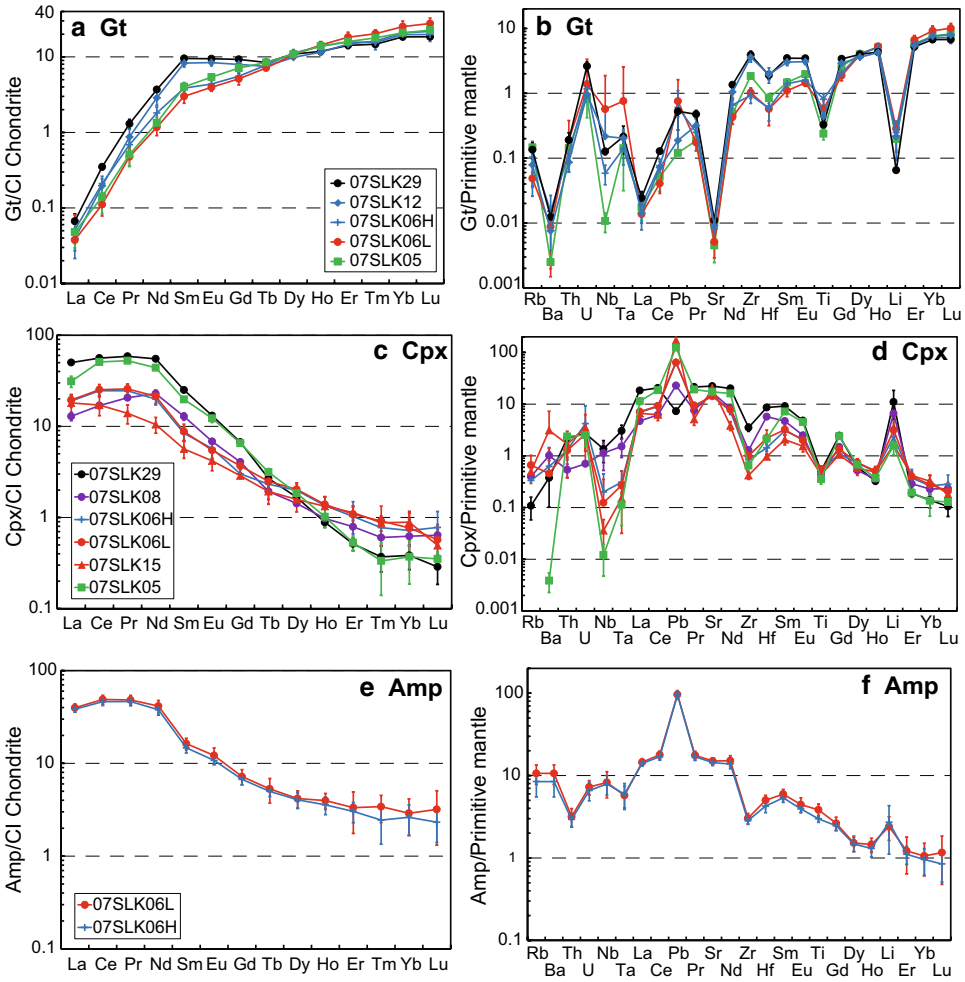

Fig. 7 REE and multi-element patterns of garnet (**a**, **b**), clinopyroxene (**c**, **d**) and amphibole (**e**, **f**) in the Shenglikou peridotite massif, normalized to the values for chondrites (for REE) and the primitive mantle (for multi-element plot) (McDonough and Sun 1995). The *error bars* are ± 1σ

The weighted average $\delta^{18}O$ values of garnet from 07SLK06L (Pyro-rich interlayer), 07SLK06H (Ol-rich interlayer) and 07SLK12 (Ol-rich block) are 5.67 ± 0.10 ‰ (n = 15, 2σ, MSWD = 1.5), 5.67 ± 0.07 ‰ (n = 16, 2σ, MSWD = 0.64) and 5.71 ± 0.10 ‰ (n = 14, 2σ, MSWD = 0.29), respectively.

Discussion

Origin as Archean refractory SCLM

The lithospheric mantle represented by orogenic peridotites usually records complex histories of physiochemical modification (e.g., Bodinier and Godard 2003 and references therein). Studies of the chemistry and Re–Os isotopic compositions of the most depleted rocks have been proven to be the best approaches to reveal the primary nature of such modified mantle domains (e.g., Alard et al. 2002; Brueckner et al. 2002; Griffin et al. 2002a, 2004; Pearson et al. 2003; Pearson and Nowell 2004; Pearson and Wittig 2008; Aulbach et al. 2009).

The Shenglikou peridotite massif is an ultramafic complex including several lithological associations, which has resulted in debates on its origin and initial formation age (e.g., Yang et al. 1994; Song et al. 2007, 2009, 2014; Yang and Powell 2008; Shi et al. 2010; Xiong et al. 2011). Yang et al. (1994) and Yang and Powell (2008) suggested that the Shenglikou peridotites were derived from a refractory lithospheric mantle wedge and experienced low-temperature seawater alteration, but did not give further age constraints on the mantle origin. Using conventional geochemical techniques, Song et al. (2007, 2009) interpreted the garnet-free dunite and harzburgite as derived from a refractory lithospheric mantle, while the garnet-bearing interlayers of dunite–harzburgite–lherzolite–pyroxenite were regarded as early Paleozoic Alaskan-type layered cumulates segregated from high-MgO mantle-wedge magmas. Subsequently, Shi et al. (2010) and Xiong et al. (2011) studied the Re–Os isotopes of whole rocks and the Lu–Hf isotopes of zircons, respectively, to show shat the Shenglikou peridotites originally formed in the Archean period and experienced Proterozoic melt metasomatism.

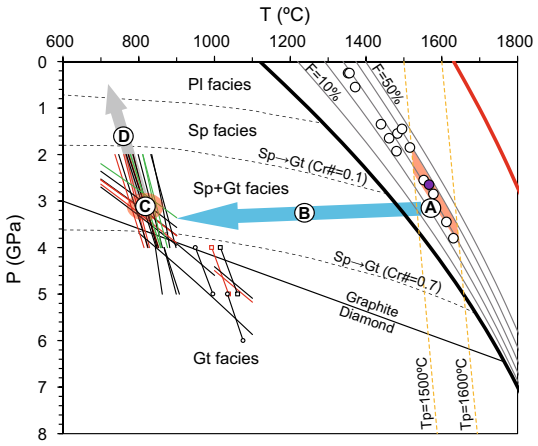

Fig. 8 *P–T* diagram showing the constraints on the Archean melting conditions (*circle* "*A*") and later pressure–temperature paths (*circles* "*B–D*") for the Shenglikou peridotite massif. The *thick red* and *black curves* represent the liquidus and anhydrous solidus of fertile lherzolite, respectively. The Archean melting pressures and temperatures derived using the method of Lee and Chin (2014) are shown as white (literature) and purple (07SLK08) circles. The *thin gray curves* show the melting *P–T* conditions corresponding to the residues after 10–50 % melt extraction. Two *yellow dashed lines* represent the adiabatic thermal state with Tp of 1600 and 1500 °C. The *pink area* constrained by the two adiabatic lines and the melting residue curves (F = ~30–40 %) shows the melting *P–T* conditions during the formation of Archean SCLM (*circle* "A"). The three thin, *black dashed lines* mark the plagioclase (Pl)-spinel (Sp) transitions in fertile mantle (Ulmer 2001), and the transitions of spinel-garnet (Gt) peridotites as a function of mantle fertility (Cr# = 0.1 and 0.7; Klemme and O'Neill 2000). The graphite–diamond transition is from Day (2012). The short *black*, *red* and *green lines* represent the *P–T* estimates for the Ol-rich peridotites, Pyro-rich peridotites and pyroxenite, respectively, using multiple barometers and thermometers (Online Resource 12). The *short lines* with *two circles* give the temperature estimates using $T_{O'NW79}$ (O'Neill and Wood 1979), while those with two squares show the results from T_{BKCa90} (Brey and Kohler 1990). The *blue arrow* with *circle* "*B*" shows the secular cooling of the SCLM from its Archean generation ("*A*") to early Paleozoic UHP recrystallization ("*C*"). The *gray arrow* from "C" to "D" indicates the decompression path when the Shenglikou massif was involved in the exhumation of the subducted Qaidam crust. Some *P–T* estimates below the graphite–diamond transition are based on mineral pairs of stages 0 and 1 (see footnotes of Online Resource 12)

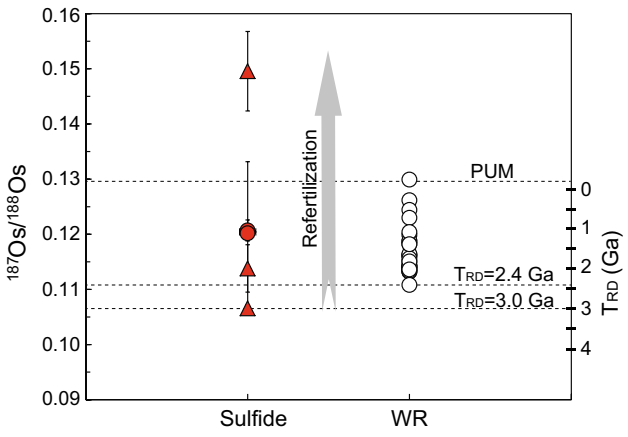

Fig. 9 Variations of $^{187}Os/^{188}Os$ ratios and T_{RD} ages relative to the ECR reservoir (Walker et al. 2002) of sulfides (this study) and whole rocks (Shi et al. 2010) from the Shenglikou peridotite massif. The *gray arrow* shows the trend of refertilization by addition of radiogenic–Os components. The oldest T_{RD} ages of sulfides (3.0 Ga) and whole rocks (2.4 Ga) are shown, respectively. PUM is from Meisel et al. (2001). The *error bars* are ± 1σ, and those without *error bars* have uncertainties less than the size of the symbol

In this study, the most refractory sample is 07SLK08 (Ol-rich group), which has an Mg# of 0.919 and an Al_2O_3 content of 1.5 wt% (Table 1). Modeling of the anhydrous fractional melting of a primitive-mantle-like source using the method of Herzberg (2004) shows that 07SLK08 is similar to a residue after ~30 % melt extraction (Fig. 3a, b). A dunite reported by Yang and Powell (2008) shows Mg# up to 0.923, Al_2O_3 down to 0.55 wt% and a CaO content of 0.10 wt%; these compositions are consistent with those of the residue produced from a primitive-mantle-like source by ~40 % anhydrous melt extraction (Herzberg 2004). The low FeO_T signature (7.2 wt%) of this dunite is consistent with an Archean origin and contrasts with the reactive dunite (~8.0 wt% or higher FeO_T) that formed in melt-peridotite reaction channels, as commonly seen in ophiolitic rocks (Bodinier and Godard 2003; Griffin et al. 2009). The lowest HREE abundances of the Shenglikou Ol-rich peridotites are ~0.01–0.5 times CI chondritic values (Figs. 3f, 4a), and their olivine Mg# and spinel Cr# can be up to 0.921 and 0.71, respectively; these characteristics also reflect the refractory nature of the Ol-rich peridotites, as extraction of ~30–40 % melts from a primitive-mantle protolith (Fig. 5c, d). These depleted whole-rock and mineral compositions in the Shenglikou Ol-rich peridotites are more similar to those of experimental products of anhydrous melting (Walter 2003), rather than an origin as accumulation from high-MgO hydrous magmas (Song et al. 2007, 2009).

Temperature–pressure modeling (Fig. 8) of anhydrous melting conditions using the method of Lee and Chin (2014), combined with the estimates of melting pressures using the method of Herzberg (2004), shows that the formation of the protolith of the Shenglikou Ol-rich peridotites (~30–40 % anhydrous melt extraction) probably occurred at ≤5 GPa and ~1600–1500 °C. These *P–T* estimates are similar to the conditions estimated for the formation of Archean SCLM elsewhere (e.g., Griffin et al. 2003; Canil 2004; Herzberg 2004; Carlson et al. 2005; Pearson and Wittig 2008; Lee et al. 2011; Lee and Chin 2014), and the temperatures are consistent with the thermal states of Archean ambient mantle (e.g., Herzberg et al. 2010).

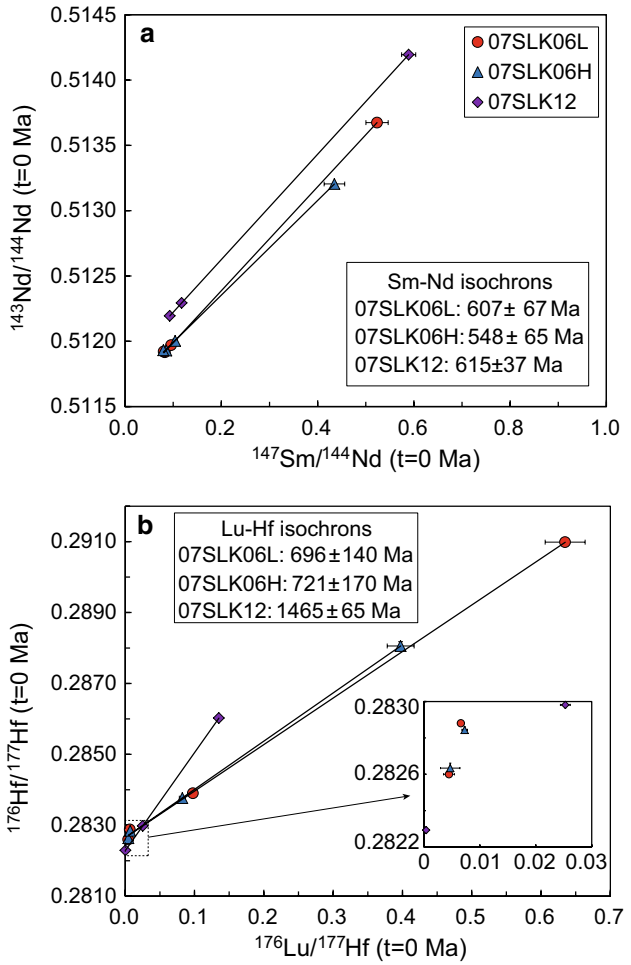

Fig. 10 Sm–Nd (**a**) and Lu–Hf (**b**) isochron diagrams of garnet, clinopyroxene and amphibole in the Shenglikou peridotite massif. *Error bars* of $\pm 1\sigma$ are shown. *Inset* in **b** shows a closer view of the data for clinopyroxene and amphibole. The isochron ages are calculated using the ISOPLOT program of Ludwig (2003)

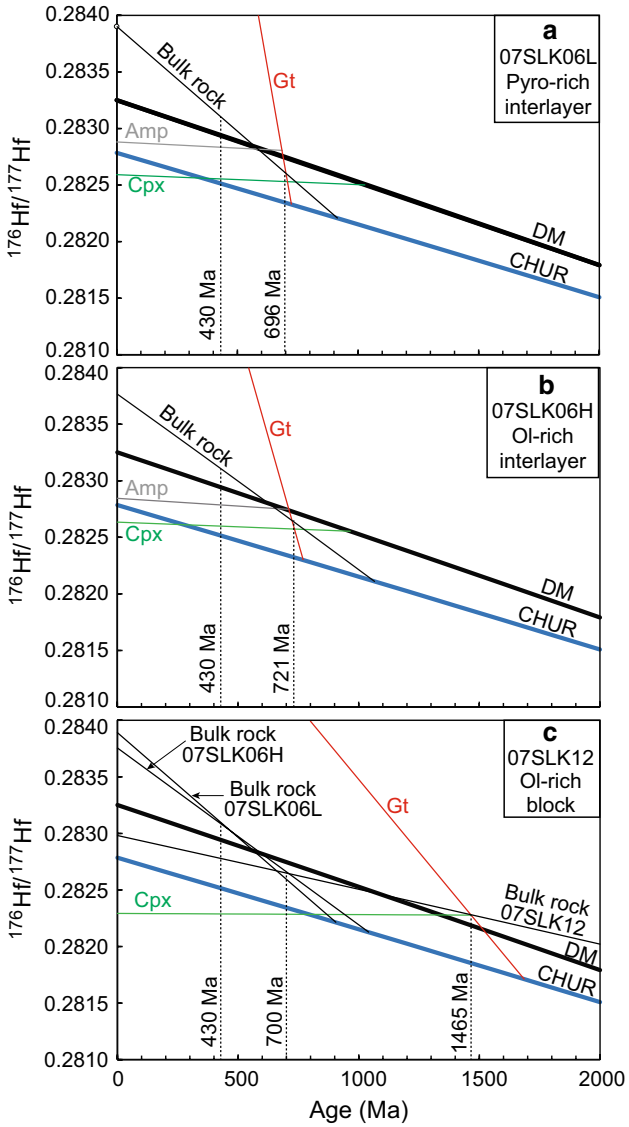

Fig. 11 Modeling of age (Ma) versus $^{176}Hf/^{177}Hf$ initial ratios for garnet (*red lines*), clinopyroxene (*green lines*), amphibole (*gray lines*) and whole rock (*black lines*) in the Shenglikou peridotite massif. The evolution paths of $^{176}Hf/^{177}Hf$ with time are modeled using the present $^{176}Lu/^{177}Hf$ and $^{176}Hf/^{177}Hf$ ratios. The *thick black* and *blue lines* represent the evolution paths of DM (Griffin et al. 2000) and CHUR (Bouvier et al. 2008), respectively. The intersections of Hf isotopic paths with the DM and CHUR lines point to the T_{DM} and T_{CHUR} model ages, respectively. In **a**–**c**, the internal isochron ages (696, 721 and 1465 Ma; *vertical dashed lines*) are indicated by the intersections of Hf isotopic paths between minerals and whole rock in each sample; the 430 Ma *vertical lines* intersect with minerals and bulk rocks at different Hf isotopic ratios, implying disequilibrium at that time. In **c**, the whole-rock Hf-isotope evolution lines for 07SLK06L and 07SLK06H are also shown; by ~700 Ma, the 07SLK12 bulk rock (Ol-rich peridotite block) had evolved to a Hf isotopic composition similar to those of 07SLK06L and 07SLK06H (interlayers of Pyro-rich and Ol-rich peridotites), suggesting the Pyro-rich layers were probably generated by refertilization of the Ol-rich peridotite blocks

Our in situ Re–Os isotopic data from sulfides show the existence of extremely unradiogenic $^{187}Os/^{188}Os$ compositions (down to 0.1066) in the Shenglikou peridotite, corresponding to a Mesoarchean T_{RD} model age (~3 Ga; Fig. 9). Although we cannot exclude the possibility that the ~3 Ga component was derived from old alloy nuggets preserved in the post-Archean convective mantle (e.g., Rudnick and Walker 2009), the whole-rock Os-isotope data give clear evidence that the refractory peridotite in this massif was generated by the formation of SCLM of at least Neoarchean age (Fig. 9; Shi et al. 2010).

All the evidence above suggests that the initial protolith of the Shenglikou peridotite massif was probably produced by a high-degree melting event (≤40 %) in the Archean

and under *P*–*T* conditions of ≤5 GPa and 1600–1500 °C, rather than being high-MgO cumulates segregated from early Paleozoic mantle-wedge magmas (Song et al. 2007, 2009).

~1.5–1.4 Ga mantle refertilization recorded by Ol-rich peridotite blocks

The most depleted rocks in the Shenglikou Ol-rich peridotites probably represent the original residues after ~30–40 % melting of primitive convective mantle (Fig. 3a, b) in the Archean thermal state, as suggested above. Experimental studies show that under anhydrous conditions, formation of this kind of refractory peridotites from the primitive mantle would consume all clinopyroxene, spinel and garnet and only leave harzburgitic assemblages at ≤3 GPa, while at ~4–5 GPa, the residues after ~30–40 % melting would have lost all clinopyroxene and most of the garnet (e.g., Walter 2003). The observed garnet and clinopyroxene modes (Online Resource 2) in most of the Shenglikou Ol-rich peridotites are too high to be explained as exsolution products from high-Al and high-Ca Opx, which can be generated by anhydrous melting at high pressures (>5 GPa) (e.g., Walter 2003; Canil 2004). Previous studies on the Archean dunites in the Western Gneiss Region of Norway have shown that after high-degree (>35 %) melting there is not enough Al and Ca left to exsolved garnet and clinopyroxene from orthopyroxene (e.g., Beyer et al. 2006). Therefore, most of the garnet and clinopyroxene in the Shenglikou Ol-rich peridotite blocks is more likely to have been introduced by refertilization of the depleted Archean protolith. A similar process has been proposed to explain the origin of excess of garnet and clinopyroxene in "depleted" peridotites from the Kaapvaal craton, Africa (e.g., Simon et al. 2003).

Because the Lu–Hf isotopic system has lower mobility in fluids and higher closure temperatures than those of the Rb–Sr and Sm–Nd systems (e.g., Blichert-Toft et al. 1999; Simon et al. 2007), we can use the Lu–Hf isotopic compositions to constrain the timing of the refertilization processes. In the Shenglikou samples, the garnet and clinopyroxene from the Ol-rich peridotite blocks have more refractory signatures (higher Mg# and Cr_2O_3; Figs. 5a, b, 6a, b) and are more enriched in highly and moderately incompatible elements (e.g., Lu and Hf; Fig. 7a–d) than those in the Pyro-rich rocks. The difference is also shown in the Lu–Hf isotopic compositions (Table 4; Figs. 10, 11).

The initial $^{176}Hf/^{177}Hf$ ratios of garnet, clinopyroxene and reconstructed bulk rock of 07SLK12 (a representative Ol-rich peridotite) show large variations from 0.28494 to 0.28229, corresponding to $\varepsilon_{Hf}(t = 430\ Ma)$ of +86 to −8 (Online Resource 13). This discrepancy implies that the Lu–Hf system in this Ol-rich peridotite did not attain internal equilibrium at 430 Ma, when the Shenglikou peridotite experienced the UHP recrystallization during the North Qaidam orogeny (e.g., Song et al. 2005a; Xiong et al. 2011, 2014). The Lu–Hf isochron age given by the garnet, clinopyroxene and bulk rock of 07SLK12 is 1465 ± 65 Ma (Fig. 10b), suggesting an early Mesoproterozoic equilibration of Lu–Hf isotopes in the Shenglikou Ol-rich peridotites. Modeling of the variation of Hf isotopic compositions with age (Fig. 11c) illustrates that the $^{176}Hf/^{177}Hf$ ratio at 1465 Ma is slightly higher than the value of depleted convective mantle at the same time. The mineral Hf T_{DM} ages that defined by the intersection of Lu–Hf isotopic evolution lines with the depleted-mantle line show Mesoproterozoic ages similar to the isochron age (Fig. 11c). This is suggestive of a depleted-mantle source for the garnet and clinopyroxene, which host most of the Lu and Hf in the bulk rock of the Shenglikou Ol-rich peridotites, as shown by the mass balance calculation (Online Resource 10). The oxygen-isotope compositions of garnet in the Shenglikou Ol-rich peridotite blocks also indicate an uncontaminated upper mantle origin (e.g., 07SLK12; $\delta^{18}O = 5.7 \pm 0.1$ ‰).

The chemical and isotopic evidence above suggests that the garnet and clinopyroxene in the Shenglikou Ol-rich peridotite blocks were probably introduced by silicate-melt metasomatism at ~1.5–1.4 Ga, superimposed on the Archean SCLM protolith of the Shenglikou massif. The refertilizing melts were likely derived from the depleted convective mantle and largely reset the bulk-rock Lu/Hf ratio to a value lower than that of the depleted-mantle reservoir (Fig. 11c). The introduced Ca- and Al-rich components formed the garnet and clinopyroxene with the same initial Hf isotopic compositions at 1465 Ma; the fractionation of Lu and Hf between garnet and clinopyroxene produced different Lu/Hf ratios and the diverse evolution paths shown in Fig. 11c.

The SCLM refertilization at ~1.5–1.4 Ga is temporally equivalent to an important episode of continental extension that generated abundant swarms of mafic dykes/sills during the breakup of the Columbia supercontinent (e.g., Ernst et al. 2008). This global-scale extension may provide a tectonic framework for the upwelling and melting of depleted convective mantle, which supplied the refertilizing magmas that deposited garnet and clinopyroxene in the protolith of the Shenglikou Ol-rich peridotite blocks.

Formation of pyroxene-rich layers by mantle refertilization at ~700 Ma

A significant feature of the Shenglikou peridotite massif is the occurrence of interlayered Pyro-rich and Ol-rich ultramafic rocks, such as 07SLK06L and 07SLK06H (Online Resource 1). The high modes of clinopyroxene and garnet (Online Resource 2) and elevated contents of basaltic

components (e.g., Al_2O_3, CaO and TiO_2; Fig. 3) in the Pyro-rich rocks are inconsistent with the latter being products of partial melting from a primitive-mantle protolith, as modeled in Fig. 3a, b. Previous investigations have suggested that they represent layered cumulates with different proportions of minerals, segregated from high-MgO mantle-wedge melts (Song et al. 2007, 2009). However, studies on other orogenic peridotites in collisional zones usually interpret similar Pyro-rich layers as the products of silicate-melt refertilization (e.g., Bodinier and Godard 2003; Beyer et al. 2006; Le Roux et al. 2007). Here, we list lines of evidence to argue the most likely genesis for the Shenglikou Pyro-rich layers.

1. In the inner garnet-bearing zones of the Shenglikou peridotite massif, decimeter- to centimeter-thick layers of Pyro-rich lherzolite, wehrlite and anhydrous clinopyroxenite occur within thick layers of Ol-rich peridotites. In a representative sample (07SLK06; Online Resource 1), garnet- and clinopyroxene-rich bands of lherzolite (07SLK06L) are interlayered within Ol-rich bands of harzburgite (07SLK06H), which randomly enclose unserpentinized clusters of Ca–Al-rich minerals similar to those in the Pyro-rich bands. The ultramafic layers show plastic shearing and oriented distribution of matrix minerals around porphyroblasts, and the foliation is the same as the direction of lithological layering. These observations are not consistent with the unstrained textures of ultramafic cumulates, such as the hydrous clinopyroxenite dykes crosscutting the Shenglikou peridotite layers (Xiong et al. 2014). Similar structural and textural relationships have also been observed in pyroxenite-veined peridotite massifs in the Alps, Betic-Rif and Dabie-Sulu belts (Bodinier and Godard 2003 and references therein), where the Pyro-rich lithologies have usually been interpreted as products of later silicate-melt additions (e.g., Beyer et al. 2006; Le Roux et al. 2007).
2. The anhydrous pyroxenite layer (07SLK05) has the most fertile oxide compositions among all the Shenglikou ultramafic rocks (Fig. 3) and shows the highest abundances of lithophile elements (such as REE; Fig. 4a). The LREE-enriched pattern of this pyroxenite suggests that it either crystallized from a LREE-enriched mafic melt or represents a trapped ultramafic melt with a LREE-enriched signature. The bulk-rock MgO contents (Fig. 3) and Mg# (0.87) imply a possible origin as ultramafic cumulates, but an origin as trapped melts is also possible [see discussion of pyroxenite origins in Xiong et al. (2014)]. The Pyro-rich peridotite layer (07SLK06L) has a more fertile major-element composition (Fig. 3) and higher abundances of lithophile elements (e.g., Y and HREE; Fig. 4) than the primitive mantle (McDonough and Sun 1995). The major- (Figs. 5, 6) and trace-element (Fig. 7) compositions of the minerals show that the Pyro-rich ultramafic rocks have less depleted features than the Ol-rich peridotites. A simple model of two-endmember mixing is shown in Fig. 3a–c; this assumes that the most depleted end member is a dunite reported by Yang and Powell (2008), and the added melt is represented by the pyroxenite (07SLK05). The modeling suggests that most of the Shenglikou Pyro-rich peridotites can be explained by 20–60 % addition of melts with the composition of 07SLK05. The similarities in chemistry (Figs. 5, 6, 7) and Sr–Nd–O isotopes (Online Resources 7, 13) of Ca–Al-rich mineral phases between 07SLK06L and 07SLK06H indicate that the added melts were mainly preserved in the Pyro-rich layers while less material was left in Ol-rich layers. The differences in Cr_2O_3, Mg# and Hf isotopes between the garnets from 07SLK06L and 07SLK06H (Fig. 5a, b; Online Resource 13) probably imply that the melt-peridotite reaction was not complete and that the garnet in 07SK06H inherited the signature from that in the Ol-rich protolith.
3. Sulfide and whole-rock Re–Os isotopic data show large variations in the Shenglikou peridotite massif, even within a single sample (e.g., 07SLK15; Fig. 9). This signature suggests that the heterogeneities of Os isotopes can be preserved on a centimeter scale in the SCLM. This kind of heterogeneity may be totally inherited from the convective mantle (e.g., Rudnick and Walker 2009), but the continuous variations of whole-rock $^{187}Os/^{188}Os$ ratios are more easily explained by incomplete reaction and mixing between melts with radiogenic Os and ancient peridotites with unradiogenic Os. An origin by accumulation from hydrous mantle-wedge magmas is hardly consistent with the large variations on Os isotopes. The Re and Pt signals and Re/Os ratios of most sulfides (>95 %) are too high to give meaningful $^{187}Os/^{188}Os$ ratios, suggesting the addition of Re and Pt with melts/fluids after the formation of Archean SCLM (e.g., Alard et al. 2002, 2011; Griffin et al. 2002a; Pearson and Nowell 2004; Aulbach et al. 2009).
4. The Lu–Hf isotopic compositions of the Pyro-rich ultramafic rocks show a more radiogenic Hf-isotope signature than the Ol-rich peridotite blocks (Online Resource 13). The modeling of Lu–Hf isotopic evolution (Fig. 11) also displays very diverse paths for the two different groups. It is very difficult to explain the large difference of Hf isotopic compositions between the Pyro-rich and Ol-rich peridotites, if they were produced by coeval accumulation in early Paleozoic (Song et al. 2007, 2009).

Therefore, we suggest that the Shenglikou Pyro-rich ultramafic layers were probably produced by different extents of silicate-melt addition into the Ol-rich peridotite blocks. The timing and the agent for this refertilization are constrained below.

The Lu–Hf isochrons defined by garnet, clinopyroxene and reconstructed bulk-rock compositions in 07SLK06L and 07SLK06H indicate internal equilibration at ~700 Ma (Fig. 10b). The modeling in Fig. 11 shows that the minerals and bulk rock in the interlayered peridotites follow similar evolution paths, consistent with their similar origin as discussed above. The initial Hf-isotope compositions of 07SLK06L and 07SLK06H at 700 Ma are undistinguishable from those of the Ol-rich peridotite blocks (07SLK12) and depleted mantle as they evolved from ca 1500 Ma to ca 700 Ma (Fig. 11c). This suggests that the refertilization that produced the Pyro-rich layers was based on the Ol-rich protolith that had been refertilized at ~1.5–1.4 Ga. The introduction of silicate melts at ~700 Ma increased the Lu/Hf of the Pyro-rich peridotites, while the Ol-rich blocks escaped the Neoproterozoic refertilization. The high Lu/Hf refertilizing agents may have been derived from a depleted convective mantle that contained garnet-rich pyroxenites or other easily fused garnet-bearing material (e.g., Pearson and Nowell 2004). The oxygen isotopes of garnet ($\delta^{18}O = 5.7 \pm 0.1$ ‰) also suggest that the refertilizing melts that formed the Pyro-rich layers were derived from the upper mantle.

Many geochronological, petrochemical and geological studies have shown that the widespread occurrence of Neoproterozoic mafic igneous rocks and extensional tectonism in NE Tibet was related to the breakup of the Rodinia supercontinent (e.g., Song et al. 2006, 2010, 2014; Lu et al. 2008; Zhang et al. 2008b, 2010; Xiong et al. 2011, 2012). The Neoproterozoic extension may have resulted in the generation of mafic magmas from upwelling asthenosphere, which not only refertilized the Shenglikou Ol-rich peridotites and formed the Pyro-rich layers, but also contributed the mafic igneous rocks of the North Qaidam Orogen (e.g., Xiong et al. 2012).

Mantle-wedge fluid metasomatism during early Paleozoic

Mantle-wedge metasomatism is commonly observed in UHP orogenic peridotites, such as those in the Dabie-Sulu belt (e.g., Zheng et al. 2005; Zhang et al. 2007), the Norwegian Caledonian belt (e.g., Scambelluri et al. 2008) and the Ulten Zone (e.g., Scambelluri et al. 2006).

In the Shenglikou peridotite massif, previous reports of exsolution (Song et al. 2005b, 2009) and inclusions of hydrous minerals (Yang and Powell 2008) within nominally anhydrous minerals, and of high water contents in olivine, orthopyroxene and garnet (Jung et al. 2013) suggested that fluid metasomatism was related to the early Paleozoic slab subduction. The phlogopite-bearing pyroxenite dykes crosscutting the Shenglikou massif have been interpreted as cumulates from primitive hydrous arc magmas that were generated during the Cambrian oceanic subduction. The intrusion of hydrous arc magmas operated through melt channels in the SCLM wedge and had little impact on the enclosing peridotites (Xiong et al. 2014).

Our observations of amphibole, phlogopite, apatite and serpentine along the cleavages of porphyroblastic clinopyroxene (Online Resource 3), and of amphibole in equilibrium with anhydrous silicates (Fig. 2i, j) show the consequences of infiltration of fluids. This is also indicated by the overall enrichment in fluid-mobile elements (e.g., Cs, Ba, U, Pb and Li) in the whole rocks (Fig. 4b) and in some major silicates both from the Ol-rich and Pyro-rich rocks (Fig. 7). The radiogenic Sr-isotope compositions of garnet, clinopyroxene and amphibole (Online Resource 13) suggest metasomatism by fluids from a relatively enriched reservoir (such as the subducted continental crust or sediments), or secular ingrowth following earlier enrichment in Rb/Sr. The mineral and bulk-rock Sm–Nd isotopes show similarly enriched signatures (Online Resource 13). Modeling of the Nd-isotope evolution with time (Online Resource 14) shows that analyzed minerals and reconstructed bulk rock of each Shenglikou sample attained Sm–Nd isotopic equilibrium at ~615–548 Ma, and the initial Nd isotopic ratios at the isochron ages were a bit lower than the CHUR line. Because the Sm/Nd ratios of bulk rocks are lower than those of DM and CHUR, they would yield enriched signatures at 430 Ma, when the Shenglikou peridotite massif underwent UHP recrystallization (P = ~3.3–2.8 GPa, T = ~846–761 °C; circle "C" in Fig. 8). The Sm–Nd isotopic characteristics can be interpreted either as the results of metasomatism by fluids liberated from the early Paleozoic subducted crustal materials or as the consequences of isotopic evolution in low Sm/Nd compositions produced by the Neoproterozoic refertilization. The latter possibility is inconsistent with the high Lu/Hf ratios of the refertilizing agents required by the depleted Hf-isotope signatures (Fig. 11). Therefore, we suggest that the Shenglikou peridotites experienced mantle-wedge metasomatism by fluids liberated from the subducted slabs during the early Paleozoic convergence of the Qaidam and Qilian blocks.

Conclusions

The Shenglikou peridotite massif in the North Qaidam Orogen (NE Tibet, China) mainly consists of pyroxene-rich and olivine-rich ultramafic rocks. Re–Os isotopic data and the highly depleted primary compositions of the rocks

and their minerals suggest an origin as Archean continental lithospheric mantle, formed by ~30–40 % melt extraction from a primitive convective mantle under *P–T* conditions of ≤5 GPa and 1600–1500 °C.

This Archean SCLM was refertilized by silicate melts sourced from the depleted asthenosphere at ~1.5–1.4 Ga; these added clinopyroxene and garnet to the olivine-rich peridotite. This event corresponds temporally to a significant extensional phase during the breakup of the Columbia supercontinent. The re-enriched SCLM was then strongly refertilized by silicate melts extracted from the depleted convective mantle at ~700 Ma, and this refertilization generated large volumes of pyroxene-rich peridotite and pyroxenite layers. The ~700-Ma refertilization was probably the deep-lithosphere response to the breakup of the Rodinia supercontinent.

The early Paleozoic convergence between the Qaidam and Qilian blocks resulted in the metasomatic overprinting of the Shenglikou peridotites by fluids from the subducting slab and led to UHP recrystallization during the North Qaidam orogeny. The long-term cooling of the SCLM (path "B" in Fig. 8) is a prerequisite for the preservation of ancient information on mantle refertilization. This study shows that the episodic refertilization and metasomatism of the Archean SCLM, temporally linked to supercontinent cycles, was an important mechanism for modification and destruction of a cratonic mantle.

Acknowledgments We thank P. Wieland, W. Powell, D. Adams and K. Grant (CCFS/GEMOC, Macquarie University) for their assistance with the major, trace element and Sr–Nd–Hf isotopic analyses and thank Drs. L. Martin and J. Cliff (CCFS/CMCA, University of Western Australia) for oxygen isotopic analyses using CAMECA SIMS 1280. This manuscript benefited greatly from the constructive and significant comments from reviewers Drs. S. Aulbach and V. Le Roux, and we thank the Editors J. Hoefs and T.L. Grove for other suggestions. This work was supported by the National Science Foundation of China (41130315 and 91214204), the Fund for Outstanding Doctoral Dissertation (CUG), ARC Discovery Project and Centre of Excellence Grants (SYO'R and WLG), a Macquarie University International Postgraduate Scholarship and a scholarship from Chinese Scholarship Council. This study used instrumentation funded by ARC LIEF and DEST Systemic Infrastructure Grants, Macquarie University. This is contribution 591 from the ARC Centre of Excellence for Core to Crust Fluid Systems (www.ccfs.mq.edu.au) and 990 from the GEMOC Key Centre (www.gemoc.mq.edu.au).

References

Alard O, Griffin WL, Pearson NJ, Lorand JP, O'Reilly SY (2002) New insights into the Re–Os systematics of sub-continental lithospheric mantle from in situ analysis of sulphides. Earth Planet Sci Lett 203:651–663

Alard O, Lorand JP, Reisberg L, Bodinier JL, Dautria JM, O'Reilly SY (2011) Volatile-rich metasomatism in Montferrier xenoliths (southern France): implications for the abundances of chalcophile and highly siderophile elements in the subcontinental mantle. J Petrol 52:2009–2045

Arai S, Ishimaru S (2008) Insights into petrological characteristics of the lithosphere of mantle wedge beneath arcs through peridotite xenoliths: a review. J Petrol 49:665–695

Aulbach S, Shirey SB, Stachel T, Creighton S, Muehlenbachs K, Harris JW (2009) Diamond formation episodes at the southern margin of the Kaapvaal Craton: Re–Os systematics of sulfide inclusions from the Jagersfontein Mine. Contrib Mineral Petrol 157:525–540

Berman RG, Aranovich LY, Pattison DRM (1995) Reassessment of the garnet-clinopyroxene Fe–Mg exchange thermometer: II. Thermodynamic analysis. Contrib Mineral Petrol 119:30–42

Beyer EE, Griffin WL, O'Reilly SY (2006) Transformation of Archaean lithospheric mantle by refertilization: evidence from exposed peridotites in the Western Gneiss Region, Norway. J Petrol 47:1611–1636

Blichert-Toft J, Albarède F, Kornprobst J (1999) Lu–Hf isotope systematics of garnet pyroxenites from Beni Bousera, Morocco: implications for basalt origin. Science 283:1303–1306

Bodinier JL, Godard M (2003) Orogenic, ophiolitic, and abyssal peridotites. In: Holland HD, Turekian KK (eds) Treatise on geochemistry, V2. Elsevier, Amsterdam, pp 103–170

Bouvier A, Vervoort JD, Patchett PJ (2008) The Lu–Hf and Sm–Nd isotopic composition of CHUR: constraints from unequilibrated chondrites and implications for the bulk composition of terrestrial planets. Earth Planet Sc Lett 273:48–57

Brey GP, Kohler T (1990) Geothermobarometry in four-phase lherzolites II. New thermobarometers, and practical assessment of existing thermobarometers. J Petrol 31:1353–1378

Brueckner HK, Carswell DA, Griffin WL (2002) Paleozoic diamonds within a Precambrian peridotite lens in UHP gneisses of the Norwegian Caledonides. Earth Planet Sci Lett 203:805–816

Canil D (2004) Mildly incompatible elements in peridotites and the origins of mantle lithosphere. Lithos 77:375–393

Carlson RW, Pearson DG, James DE (2005) Physical, chemical, and chronological characteristics of continental mantle. Rev Geophys. doi:10.1029/2004RG000156

Chen NS, Gong SL, Sun M, Li XY, Xia XP, Wang QY, Wu FY, Xu P (2009a) Precambrian evolution of the Quanji Block, northeastern margin of Tibet: insights from zircon U–Pb and Lu–Hf isotope compositions. J Asian Earth Sci 35:367–376

Chen DL, Liu L, Sun Y, Liou JG (2009b) Geochemistry and zircon U–Pb dating and its implications of the Yukahe HP/UHP terrane, the North Qaidam, NW China. J Asian Earth Sci 35:259–272

Condie KC (1998) Episodic continental growth and supercontinents: a mantle avalanche connection? Earth Planet Sci Lett 163:97–108

Day HW (2012) A revised diamond-graphite transition curve. Am Mineral 97:52–62

DePaolo DJ (1981) Neodymium isotopes in the Colorado Front Range and crust–mantle evolution in the Proterozoic. Nature 291:193–196

Dick HJB , Bullen T (1984) Chromian spinel as a petrogenetic indicator in abyssal and alpine-type peridotites and spatially associated lavas. Contrib Mineral Petrol 86:54–76

Downes H (2001) Formation and modification of the shallow sub-continental lithospheric mantle: a review of geochemical evidence from ultramafic xenolith suites and tectonically emplaced ultramafic massifs of western and central Europe. J Petrol 42:233–250

Ellis DJ, Green DH (1979) An experimental study of the effect of Ca upon garnet-clinopyroxene Fe–Mg exchange equilibria. Contrib Mineral Petrol 71:13–22

Ernst RE, Wingate MTD, Buchan KL, Li ZX (2008) Global record of 1600–700 Ma Large Igneous Provinces (LIPs): implications for the reconstruction of the proposed Nuna (Columbia) and Rodinia supercontinents. Precambrian Res 160:159–178

Foley SF (2008) Rejuvenation and erosion of the cratonic lithosphere. Nat Geosci 1:503–510

Gao S, Rudnick RL, Carlson RW, McDonough WF, Liu SY (2002) Re–Os evidence for replacement of ancient mantle lithosphere beneath the North China craton. Earth Planet Sci Lett 198:307–322

Griffin WL, Pearson NJ, Belousova E, Jackson SE, Van Achterbergh E, O'Reilly SY, Shee SR (2000) The Hf isotope composition of cratonic mantle: LAM-MC-ICPMS analysis of zircon megacrysts in kimberlites. Geochim Cosmochim Acta 64:133–147

Griffin WL, Spetsius ZV, Pearson NJ, O'Reilly SY (2002a) In situ Re–Os analysis of sulfide inclusions in kimberlitic olivine: new constraints on depletion events in the Siberian lithospheric mantle. Geochem Geophys Geosyst 3:1069. doi:10.1029/2001GC000287

Griffin WL, Fisher NI, Freidman JH, O'Reilly SY, Ryan CG (2002b) Cr-pyrope garnets in the lithospheric mantle 2. Compositional populations and their distribution in time and space. Geochem Geophys Geosyst. doi:10.1029/2002GC000298

Griffin WL, O'Reilly SY, Abe N, Aulbach S, Davies RM, Pearson NJ, Doyle BJ, Kivi K (2003) The origin and evolution of Archean lithospheric mantle. Precambrian Res 127:19–41

Griffin WL, Graham S, O'Reilly SY, Pearson NJ (2004) Lithosphere evolution beneath the Kaapvaal Craton: Re–Os systematics of sulfides in mantle-derived peridotites. Chem Geol 208:89–118

Griffin WL, O'Reilly SY, Afonso JC, Begg GC (2009) The composition and evolution of lithospheric mantle: a re-evaluation and its tectonic implications. J Petrol 50:1185–1204

Haggerty SE, Tompkins LA (1983) Redox state of Earth's upper mantle from kimberlitic ilmenites. Nature 303:295–300

Hawkesworth CJ, Kemp AIS (2006) Evolution of the continental crust. Nature 443:811–817

Herzberg C (2004) Geodynamic information in peridotite petrology. J Petrol 45:2507–2530

Herzberg C, Condie K, Korenaga J (2010) Thermal history of the Earth and its petrological expression. Earth Planet Sci Lett 292:79–88

Jordan TH (1978) Composition and development of the continental tectosphere. Nature 274:544–548

Jung H, Lee J, Ko B, Jun S, Park M, Cao Y, Song SG (2013) Natural type-C olivine fabrics in garnet peridotites in North Qaidam UHP collision belt, NW China. Tectonophysics 594:91–102

Klemme S, O'Neill HSC (2000) The near-solidus transition from garnet lherzolite to spinel lherzolite. Contrib Mineral Petrol 138:237–248

Le Roux V, Bodinier JL, Tommasi A, Alard O, Dautria JM, Vauchez A, Riches AJV (2007) The Lherz spinel lherzolite: refertilized rather than pristine mantle. Earth Planet Sci Lett 259:599–612

Lee CTA, Chin EJ (2014) Calculating melting temperatures and pressures of peridotite protoliths: implications for the origin of cratonic mantle. Earth Planet Sci Lett 403:273–286

Lee CTA, Luffi P, Chin EJ (2011) Building and destroying continental mantle. Annu Rev Earth Plant Sci 39:59–90

Liou JG, Zhang RY, Ernst WG (2007) Very high-pressure orogenic garnet peridotites. Proc Natl Acad Sci USA 104:9116–9121

Lu SN, Li HK, Zhang CL, Niu GH (2008) Geological and geochronological evidence for the Precambrian evolution of the Tarim Craton and surrounding continental fragments. Precambrian Res 160:94–107

Ludwig KR (2003) User's Manual for Isoplot 3.0: A Geochronological Toolkit for Microsoft Excel. Berkeley Geochronology Center, Berkeley

Mattinson CG, Wooden JL, Liou JG, Bird DK, Wu CL (2006) Age and duration of eclogite-facies metamorphism, North Qaidam HP/UHP terrane, western China. Am J Sci 306:683–711

McDonough WF, Sun SS (1995) The composition of the Earth. Chem Geol 120:223–253

Meisel T, Walker RJ, Irving AJ, Lorand JP (2001) Osmium isotopic compositions of mantle xenoliths: a global perspective. Geochim Cosmochim Acta 65:1311–1323

Nickel KG, Green DH (1985) Empirical geothermobarometry for garnet peridotites and implications for the nature of the lithosphere, kimberlites and diamonds. Earth Planet Sci Lett 73:158–170

O'Neill HSC, Wood BJ (1979) An experimental study of Fe–Mg partitioning between garnet and olivine and its calibration as a geothermometer. Contrib Mineral Petrol 70:59–70

O'Reilly SY, Griffin WL, Poudjom Djomani YH, Morgan P (2001) Are lithospheres forever? Tracking changes in subcontinental lithospheric mantle through time. GSA Today 4:4–10

Pearce JA, Barker PF, Edwards SJ, Parkinson IJ, Leat PT (2000) Geochemistry and tectonic significance of peridotites from the South Sandwich arc-basin system, South Atlantic. Contrib Mineral Petrol 139:36–53

Pearson DG, Nowell GM (2004) Re–Os and Lu–Hf isotope constraints on the origin and age of pyroxenites from the Beni Bousera peridotite massif: implications for mixed peridotite–pyroxenite mantle sources. J Petrol 45:439–455

Pearson DG, Wittig N (2008) Formation of Archean continental lithosphere and its diamonds: the root of the problem. J Geol Soc Lond 165:895–914

Pearson DG, Canil D, Shirey SB (2003) Mantle samples included in volcanic rocks: xenoliths and diamonds. In: Holland HD, Turekian KK (eds) Treatise on geochemistry, V2. Elsevier, Amsterdam, pp 171–275

Rudnick RL, Walker RJ (2009) Interpreting ages from Re-Os isotopes in peridotites. Lithos 112S:1083–1095

Scambelluri M, Hermann J, Morten L, Rampone E (2006) Melt-versus fluid-induced metasomatism in spinel to garnet wedge peridotites (Ulten Zone, Eastern Italian Alps): clues from trace element and Li abundances. Contrib Mineral Petrol 151:372–394

Scambelluri M, Pettke T, van Roermund HLM (2008) Majoritic garnets monitor deep subduction fluid flow and mantle dynamics. Geology 36:59–62

Scherer E, Münker C, Mezger K (2001) Calibration of the lutetium–hafnium clock. Science 293:683–687

Shi RD, Griffin WL, O'Reilly SY, Zhao GC, Huang QS, Li J, Xu JF (2010) Evolution of the Lüliangshan garnet peridotites in the North Qaidam UHP belt, Northern Tibetan Plateau: constraints from Re–Os isotopes. Lithos 117:307–321

Shirey SB, Walker RJ (1998) The Re–Os isotope system in cosmochemistry and high-temperature geochemistry. Annu Rev Earth Plant Sci 26:423–500

Simon NSC, Irvine GJ, Davies GR, Pearson DG, Carlson RW (2003) The origin of garnet and clinopyroxene in "depleted" Kaapvaal peridotites. Lithos 71:289–322

Simon NSC, Carlson RW, Pearson DG, Davies GR (2007) The origin and evolution of the Kaapvaal cartonic lithospheric mantle. J Petrol 48:589–625

Song SG, Zhang LF, Niu YL (2004) Ultra-deep origin of garnet peridotite from the North Qaidam ultrahigh-pressure belt, Northern Tibetan Plateau, NW China. Am Mineral 89:1330–1336

Song SG, Zhang LF, Niu YL, Su L, Jian P, Liu DY (2005a) Geochronology of diamond-bearing zircons from garnet peridotite in the North Qaidam UHPM belt, Northern Tibetan Plateau: a record of complex histories from oceanic lithosphere subduction to continental collision. Earth Planet Sci Lett 234:99–118

Song SG, Zhang LF, Chen J, Liou JG, Niu YL (2005b) Sodic amphibole exsolutions in garnet from garnet-peridotite, North Qaidam UHPM belt, NW China: implications for ultradeep-origin and hydroxyl defects in mantle garnets. Am Mineral 90:814–820

Song SG, Zhang LF, Niu YL, Su L, Song B, Liu DY (2006) Evolution from oceanic subduction to continental collision: a case study

from the northern Tibetan plateau based on geochemical and geochronological data. J Petrol 47:435–455

Song SG, Su L, Niu YL, Zhang LF, Zhang GB (2007) Petrological and geochemical constraints on the origin of garnet peridotite in the North Qaidam ultrahigh-pressure metamorphic belt, northwestern China. Lithos 96:243–265

Song SG, Niu YL, Zhang LF, Bucher K (2009) The Luliangshan garnet peridotite massif of the North Qaidam UHPM belt, NW China—a review of its origin and metamorphic evolution. J Metamorph Geol 27:621–638

Song SG, Su L, Li XH, Zhang GB, Niu YL, Zhang LF (2010) Tracing the 850-Ma continental flood basalts from a piece of subducted continental crust in the North Qaidam UHPM belt, NW China. Precambrian Res 183:805–816

Song SG, Su L, Li XH, Niu YL, Zhang LF (2012) Grenville-age orogenesis in the Qaidam-Qilian block: the link between South China and Tarim. Precambrian Res 220–221:9–22

Song SG, Niu YL, Su L, Zhang C, Zhang LF (2014) Continental orogenesis from ocean subduction, continent collision/subduction, to orogen collapse, and orogen recycling: the example of the North Qaidam UHPM belt, NW China. Earth Sci Rev 129:59–84

Spengler D, van Roermund HLM, Drury MR, Ottolini L, Mason PRD, Davies GR (2006) Deep origin and hot melting of an Archaean orogenic peridotite massif in Norway. Nature 440:913–917

Steiger RH, Jäger E (1977) Subcommission on geochronology: convention on the use of decay constants in geo- and cosmochronology. Earth Planet Sci Lett 36:359–362

Ulmer P (2001) Partial melting in the mantle wedge—the role of H_2O in the genesis of mantle-derived 'arc-related' magmas. Phys Earth Planet Inter 127:215–232

Walker RJ, Horan MF, Morgan JW, Becker H, Grossman JN, Rubin AE (2002) Comparative ^{187}Re–^{187}Os systematics of chondrites: implications regarding early solar system processes. Geochim Cosmochim Acta 66:4187–4201

Walter MJ (2003) Melt extraction and compositional variability in mantle lithosphere. In: Holland HD, Turekian KK (eds) Treatise on geochemistry, V2. Elsevier, Amsterdam, pp 363–394

Wells PRA (1977) Pyroxene thermometry in simple and complex systems. Contrib Mineral Petrol 62:129–139

Wu CL, Gao YH, Wu SP, Chen QL, Wooden JL, Mazadab FK, Mattinson C (2007) Zircon SHRIMP U–Pb dating of granites from the Da Qaidam area in the north margin of Qaidam basin, NW China. Acta Petrol Sin 23(8):1861–1875 (in Chinese with English abstract)

Xiao WJ, Windley BF, Yong Y, Yan Z, Yuan C, Liu CZ, Li JL (2009) Early Paleozoic to Devonian multiple-accretionary model for the Qilian Shan, NW China. J Asian Earth Sci 35:323–333

Xiong Q, Zheng JP, Griffin WL, O'Reilly SY, Zhao JH (2011) Zircons in the Shenglikou ultrahigh-pressure garnet peridotite massif and its country rocks from the North Qaidam terrane (western China): meso-Neoproterozoic crust-mantle coupling and early Paleozoic convergent plate-margin processes. Precambrian Res 187:33–57

Xiong Q, Zheng JP, Griffin WL, O'Reilly SY, Pearson NJ (2012) Decoupling of U–Pb and Lu–Hf isotopes and trace elements in zircon from the UHP North Qaidam orogen, NE Tibet (China): tracing the deep subduction of continental blocks. Lithos 155:125–145

Xiong Q, Zheng JP, Griffin WL, O'Reilly SY, Pearson NJ (2014) Pyroxenite dykes in orogenic peridotite from North Qaidam (NE Tibet, China) track metasomatism and segregation in the mantle wedge. J Petrol 55:2347–2376

Xu YG (2001) Thermo-tectonic destruction of the Archaean lithospheric keel beneath the Sino-Korean craton in China: evidence, timing and mechanism. Phys Chem Earth (A) 26:747–757

Yang JJ, Powell R (2008) Ultrahigh-pressure garnet peridotites from the devolatilization of sea-floor hydrated ultramafic rocks. J Metamorph Geol 26:695–716

Yang JJ, Zhu H, Deng JF, Lai SC, Zhou TZ (1994) The discovery of garnet peridotite in Northern Chaidam Mountains and its significance. Acta Petrol Mineral 13(2):97–105 (in Chinese with English abstract)

Yang JS, Xu ZQ, Zhang JX, Song SG, Wu CL, Shi RD, Li HB, Brunel M (2002) Early Palaeozoic North Qaidam UHP metamorphic belt on the north-eastern Tibetan plateau and a paired subduction model. Terra Nova 14:397–404

Yin A, Harrison TM (2000) Geologic evolution of the Himalayan-Tibetan orogen. Annu Rev Earth Pl Sc 28:211–280

Yin A, Manning CE, Lovera O, Menold CA, Chen XH, Gehrels GE (2007a) Early Paleozoic tectonic and thermomechanical evolution of ultrahigh-pressure (UHP) metamorphic rocks in the northern Tibetan Plateau, Northwest China. Int Geol Rev 49:681–716

Yin A, Dang YQ, Zhang M, McRivette MW, Burgess WP, Chen XH (2007b) Cenozoic tectonic evolution of Qaidam basin and its surrounding regions (part 2): wedge tectonics in southern Qaidam basin and the Eastern Kunlun Range. Geol Soc Am Spec 433:369–390

Zhang HF (2005) Transformation of lithospheric mantle through peridotite-melt reaction: a case of Sino-Korean craton. Earth Planet Sci Lett 237:768–780

Zhang RY, Li T, Rumble D, Yui TF, Li L, Yang JS, Pan Y, Liou JG (2007) Multiple metasomatism in Sulu ultrahigh-P garnet peridotite constrained by petrological and geochemical investigations. J Metamorph Geol 25:149–164

Zhang GB, Song SG, Zhang LF, Niu YL (2008a) The subducted oceanic crust within continental-type UHP metamorphic belt in the North Qaidam, NW China: evidence from petrology, geochemistry and geochronology. Lithos 104:99–118

Zhang JX, Mattinson CG, Meng FC, Wan YS, Tung K (2008b) Polyphase tectonothermal history recorded in granulitized gneisses from the north Qaidam HP/UHP metamorphic terrane, western China: evidence from zircon U–Pb geochronology. Geol Soc Am Bull 120:732–749

Zhang JX, Mattinson CG, Yu SY, Li JP, Meng FC (2010) U–Pb zircon geochronology of coesite-bearing eclogites from the southern Dulan area of the North Qaidam UHP terrane, northwestern China: spatially and temporally extensive UHP metamorphism during continental subduction. J Metamorph Geol 28:955–978

Zheng JP, O'Reilly SY, Griffin WL, Lu FX, Zhang M (1998) Nature and evolution of Cenozoic lithospheric mantle beneath Shandong Peninsula, Sino-Korean craton, eastern China. Int Geol Rev 40:471–499

Zheng JP, O'Reilly SY, Griffin WL, Lu FX, Zhang M, Pearson NJ (2001) Relict refractory mantle beneath the eastern North China block: significance for lithosphere evolution. Lithos 57:43–66

Zheng JP, Zhang RY, Griffin WL, Liou JG, O'Reilly SY (2005) Heterogeneous and metasomatized mantle recorded by trace elements in minerals of the Donghai garnet peridotites, Sulu UHP terrane, China. Chem Geol 221:243–259

Zheng JP, Griffin WL, O'Reilly SY, Yu CM, Zhang HF, Pearson N, Zhang M (2007) Mechanism and timing of lithospheric modification and replacement beneath the eastern North China Craton: peridotitic xenoliths from the 100 Ma Fuxin basalts and a regional synthesis. Geochim Cosmochim Acta 71:5203–5225

Zheng JP, Sun M, Griffin WL, Zhou MF, Zhao GC, Robinson P, Tang HY, Zhang ZH (2008) Age and geochemistry of contrasting peridotite types in the Dabie UHP belt, eastern China: petrogenetic and geodynamic implications. Chem Geol 247:282–304

Zheng JP, Tang HY, Xiong Q, Griffin WL, O'Reilly SY, Pearson N, Zhao JH, Wu YB, Zhang JF, Liu YS (2014) Linking continental deep subduction with destruction of a cratonic margin: strongly reworked North China SCLM intruded in the Triassic Sulu UHP belt. Contrib Mineral Petrol 167:1028. doi:10.1007/s00410-014-1028-0

Zheng JP, Lee CTA, Lu JG, Zhao JH, Wu YB, Xia B, Li XY, Zhang JF, Liu YS (2015) Refertilization-driven destabilization of subcontinental mantle and the importance of initial lithospheric thickness for the fate of continents. Earth Planet Sci Lett 409:225–231

Zindler A, Hart S (1986) Chemical geodynamics. Annu Rev Earth Plant Sci 14:493–571